atmosphere

MDPI

Article

Forecasting In-Flight Icing over Greece: Insights from a Low-Pressure System Case Study

Petroula Louka [1,*], Ioannis Samos [2,3] and Flora Gofa [3]

[1] Department of Mathematics and Natural Science, Hellenic Air Force Academy, Dekelia Air Force Base Military Post 1010, 13671 Acharnes Attiki, Greece
[2] Section of Environmental Physics and Meteorology, Department of Physics, National and Kapodistrian University of Athens, 15772 Athens, Greece; ioannis.samos@phys.uoa.gr
[3] Hellenic National Meteorological Service, 16777 Hellinikon, Greece; fgofa@hnms.gr
* Correspondence: petroula.louka@hafa.haf.gr

Abstract: Forecasting in-flight icing conditions is crucial for aviation safety, particularly in regions with variable and complex meteorological configurations, such as Greece. Icing accretion onto the aircraft's surfaces is influenced by the presence of supercooled water in subfreezing environments. This paper outlines a methodology of forecasting icing conditions, with the development of the Icing Potential Algorithm that takes into consideration the meteorological scenarios related to icing accretion, using state-of-the-art Numerical Weather Prediction model results, and forming a fuzzy logic tree based on different membership functions, applied for the first time over Greece. The synoptic situation of an organized low-pressure system passage, with occlusion, cold and warm fronts, over Greece that creates dynamically significant conditions for icing formation was investigated. The sensitivity of the algorithm was revealed upon the precipitation, cloud type and vertical velocity effects. It was shown that the greatest icing intensity is associated with single-layer ice and multi-layer clouds that are comprised of both ice and supercooled water, while convectivity and storm presence lead to also enhancing the icing formation. A qualitative evaluation of the results with satellite, radar and METAR observations was performed, indicating the general agreement of the method mainly with the ground-based observations.

Keywords: in-flight icing; Icing Potential Algorithm; NWP model results; vertical velocity; cloud top height and phase; convective activity

check for updates

Citation: Louka, P.; Samos, I.; Gofa, F. Forecasting In-Flight Icing over Greece: Insights from a Low-Pressure System Case Study. *Atmosphere* **2024**, *15*, 990. https://doi.org/10.3390/atmos15080990

Academic Editor: Pak-Wai Chan

Received: 10 July 2024
Revised: 4 August 2024
Accepted: 8 August 2024
Published: 17 August 2024

Copyright: © 2024 by the authors. Licensee MDPI, Basel, Switzerland. This article is an open access article distributed under the terms and conditions of the Creative Commons Attribution (CC BY) license (https://creativecommons.org/licenses/by/4.0/).

1. Introduction

In-flight icing has been recognized as a major hazard for aviation safety since several decades ago, as 803 aviation accidents were reported in the continental USA between 1975 and 1988 [1]. Icing affects the aerodynamic structure of the aircraft, its induction system and the operation of the sensors laying on the aircraft's surfaces. This paper focuses on structural icing, which alters the aerodynamic characteristics of the aircraft and changes the intensity of the forces acting on the aircraft, namely, the lift, thrust and drag forces, as well as the weight of the aircraft, influencing its static stability and thus increasing the stall speed [2].

The accretion of ice onto the aircraft's surfaces depends upon specific meteorological parameters and is related mainly with air temperatures below 0 °C and the presence of supercooled water droplets (SWDs), either within subfreezing clouds through collision and coalescence processes or from precipitating water in the freezing rain formation process. SWDs can be found in the range of temperatures between 0 °C and −20 °C (e.g., [1,3]), although they can be found in clouds at temperatures down to about −38 °C [4]. A recent satellite study has reported the presence of SWDs within different cloud types depending on their temperature, namely, in low clouds down to −23 °C, middle clouds down to −38 °C and high and deep convective clouds in ranges between −10 °C and −40 °C [5].

The collision–coalescence process is important in the formation of SWDs in the deep convection that is associated with significant icing formation as well as other important aviation hazards, such as turbulence and strong wind shear. Deep convective clouds are related with rather low temperatures and large droplets that rapidly produce SWDs due to strong updrafts and high supersaturation. In the case of the freezing precipitation, as snow falls and melts, liquid droplets are created in the warm air of the frontal zone. The presence of the cold subfreezing air beneath the warm air leads to supercooling and hence the formation of freezing precipitation, a procedure that mainly depends upon the vertical thermodynamic conditions. Reports from the National Transportation Safety Board (NTSB) and Aviation Safety Reporting System (ASRS) databases recorded 1202 icing related accidents and incidents in the USA over the period from 1978 to 2010 [2]. A large percentage of those events was attributed to different types of precipitation, with snow and freezing precipitation being the most significant (32.8%) [6].

At the same time, icing is influenced by the size and the concentration of the water droplets in the cloud. The icing risk increases when the SWD content is high and when droplets with diameters greater than 30 μm are present (e.g., [3,7]). In general, the size of the SWDs reported in clouds with continuous icing conditions is 40 μm in diameter and is 50 μm for intermittent icing [8]. Tcn 50 μm is a serious threat to flight as they freeze on the airframe [9,10]. In cumuliform clouds, SWDs tend to have a larger size than in stratiform clouds, and clouds in continental areas have smaller droplets than maritime areas. Droplet size as well as liquid water content generally increases with altitude in single cloud layers. Studies have shown that, in warm subfreezing clouds, the cloud top temperature (CTT) is below 0 °C but greater than −12 °C and the diameter of the SWDs is usually large, sometimes greater than 100 μm, with the liquid water content being greater than 0.5 g/m^3 [8]. The liquid water content is generally in the order of <0.5–0.7 g/m^3 in convective clouds, although it can reach higher values in deep convective clouds (~2.4 g/m^3) and <0.3–0.5 g/m^3 in stratiform clouds [10]. The type of icing (clear, rime or mixed) is determined by the size of the cloud droplets (e.g., [1]). Pilot reports (PIREPs) have also shown that the maximum probability of icing formation is at altitudes of approximately 10,000 ft, with more than 50% of the cases laying between 5000 ft and 13,000 ft [1].

Hence, in-flight icing formation is a multi-scale problem as it involves processes that take place in cloud scale and mesoscale and control the amount and distribution of water droplets, while synoptic weather patterns produce the necessary meteorological conditions that govern the location and motion of icing areas [10]. Such weather conditions are associated with frontal zones and the development of cumuliform and/or stratiform clouds. Especially in the case of convective conditions, meteorological factors such as vertical updrafts and/or embedded convection are known to be important conditions for icing accretion [11]. This complexity makes the diagnosis and forecasting of the icing events a challenging problem, as it requires understanding the physical procedures governing icing formation, quantifying accurately the severity of each meteorological condition that can be attributed as a source of influence and analyzing the available data in order to characterize and evaluate dynamic icing areas.

Forecasting in-flight icing formation and intensity is a challenging problem due to the complexity of the physics procedures in different scales. In practice, high resolution Numerical Weather Prediction (NWP) models are used to provide the necessary cloud data resulting from their microphysical schemes, such as cloud liquid water, rainwater and cloud droplet concentration, together with sophisticated precipitation and boundary layer parameterization schemes. However, no NWP model may provide direct forecasts of the specific areas, levels and intensity of icing. For this reason, the operational forecast of icing involves NWP model outputs, remote sensing and ground observations all combined through algorithms developed by various forecasting centers. These algorithms incorporate ways to describe, as closely as possible, the physical processes associated with the presence of SWDs and their effect on potential icing formation and severity (e.g., [2,12–15]).

The diagnosis, rather than the prediction, of icing from these algorithms is mainly evaluated using PIREPs, which provide trusted observations for statistical validation, while remote sensing data are used in compliment to the PIREPs (e.g., [2,13,15,16]). However, it should be noted that there are also non-meteorological factors that influence the in-flight icing, namely the type of the aircraft, its speed, and the duration it spends in a potential icing environment. These factors are not taken into account by the algorithms used and consequently in the validation process [15].

This paper focuses on the study of the effect of a well-organized depression system associated with occluded, cold and warm fronts on in-flight icing formation over Greece. This is achieved with the development and application of the Icing Potential Algorithm, applied for the first time over Greece. It must be noted that PIREP databases, which are an important tool for providing weather information at flight levels, especially for atmospheric conditions that cannot be easily observed from the ground, such as turbulence, icing and cloud heights, are generally absent for retrieval over Greece. Hence, this study performs a qualitative evaluation of the results through the available remote sensing and ground observations. To the knowledge of the authors, this is the first application of an icing algorithm over Greece, while the icing operational forecasting is based on the level of the 0 °C isotherm that is taken from NWP models, which can provide some useful information about icing conditions in the atmosphere, but it alone may not be adequate for determining all icing conditions comprehensively. Understanding and forecasting atmospheric icing potential helps reduce the risk of icing-related incidents and ensures more efficient flight planning. This is particularly relevant for regions with significant aviation traffic, such as Greece, where both commercial and general aviation operations must navigate varying weather conditions. Hence, the application and evaluation of such a method for predicting in-flight icing formation over this area is scientifically significant in terms of identifying the effect of certain meteorological parameters for which in-flight icing accretion becomes severe, especially for weather conditions, such as a low-pressure system with the accompanied fronts, which may often occur in a region.

The following sections of this paper include a description of the proposed method, presenting the Icing Potential Algorithm's development and structure and the numerical approach of its calculation and scenarios, incorporating the effect of the weather conditions and the sensitivity of the algorithm on certain meteorological parameters, a brief description of the NWP model used to extract the necessary forecasts for the algorithm's input, as well as the observations from the available sources of data employed to evaluate the outcome of the algorithm (Section 2). It further discusses the meteorological synoptic conditions for which the method is applied, presents the products of the algorithm (which are the cloud presence, i.e., cloud mask, cloud base and top height, and the corresponding temperature over the area of Greece) and analyzes the icing presence field that resulted by taking into account the different meteorological scenarios investigated (Section 3). Section 4 makes a qualitative evaluation of the results of the proposed method based on comparisons of the algorithm's outcome with the available observations, while the conclusions of the work, together with suggestions for the use of the method in future work, are presented in Section 5.

2. Data and Algorithm

This section describes the algorithm applied for the estimation of the icing potential over Greece. The data used for this application include NWP data for the initiation and calculations, while, in the absence of PIREP database retrieval over Greece, the analysis and evaluation are based on available satellite, radar and point observations.

2.1. The In-Flight Icing Potential Algorithm

The Icing Potential Algorithm (IPA) developed for the present work to estimate the in-flight icing is based on the Forecast Icing Potential (FIP) algorithm developed at the National Center for Atmospheric Research (NCAR) [8,12]. In particular, the IPA calculates

the capacity of the atmosphere to develop icing at a given flight level in favorable meteorological conditions. It uses the structure of the FIP algorithm, whichinvolves several key components and steps, and a fussy logic method to handle the inherent uncertainties and complexities in predicting in-flight icing conditions, as initially proposed by [4]. This method enables the definition of the FIP in different possible icing conditions, starting from the estimation of the formation of clouds and type of precipitation occurrence for various mixed meteorological situations and scenarios.

Specifically, the IPA uses as input weather parameter predictions derived from the NWP model COSMO-GR (COnsortium for Small-scale MOdeling), which consists of the prognostic fields of air temperature (T) and relative humidity (RH) at different flight levels from 1000 to 40,000 ft, the 2 m temperature (T2m), total precipitation (TP), convective (CS) and long-range snowfall (LS), vertical wind velocity (ω), cloud liquid water content (CLWC) and freezing level. Following [12], the IPA begins with analyzing the modeled RH and T values in order to diagnose the presence of clouds in the atmosphere and to define the highest cloud top (CTH) and its temperature (CTT) as well as the cloud base (CBH) and the corresponding cloud base temperature (CBT).

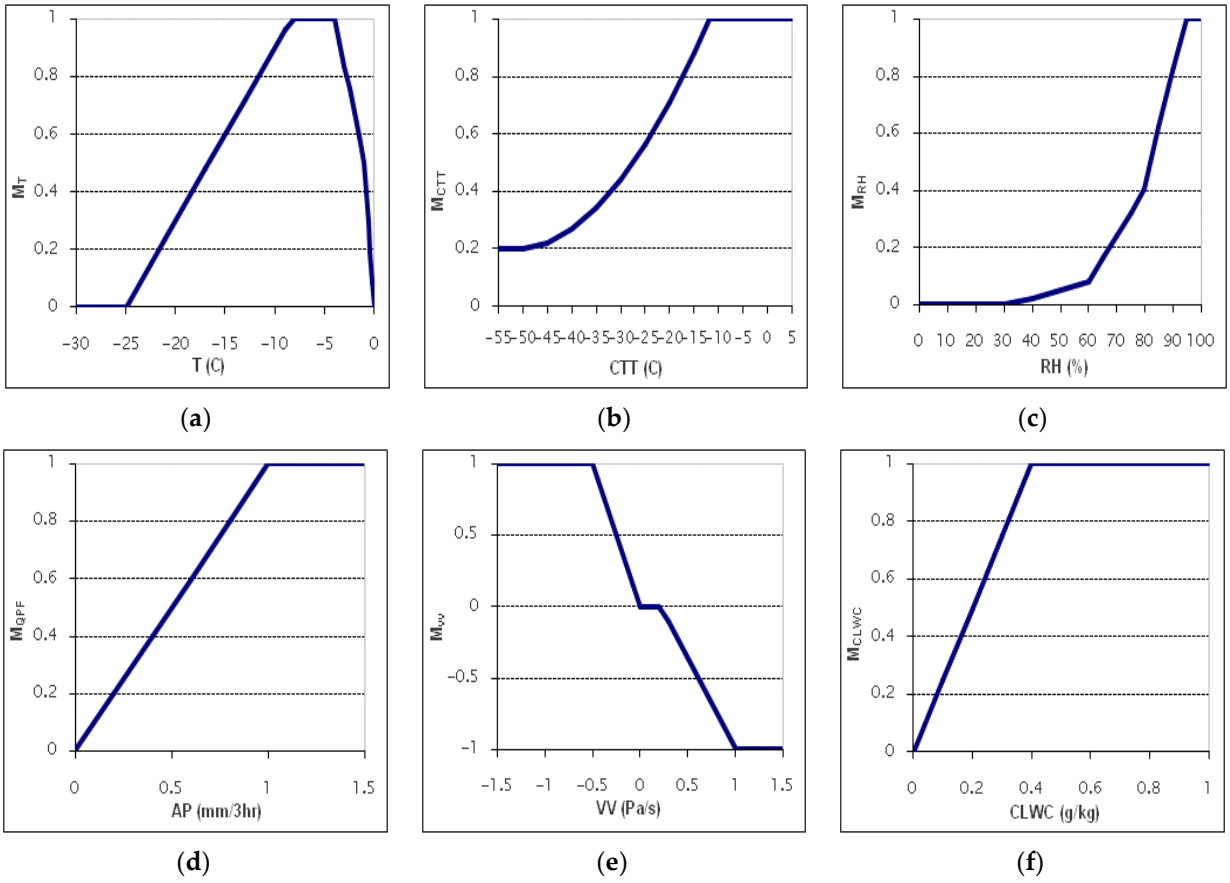
All previous works estimating in-flight icing potential used membership functions, producing interest maps showing the potential icing formation's dependence on different meteorological parameters, such as temperature (M_T), relative humidity (M_{RH}), cloud top temperature (M_{CTT}), accumulative precipitation rate (M_P), vertical velocity (M_{vv}) and cloud liquid water content (M_{CLWC}), that are mainly based on cloud physics principles, forecasting, research and PIREP observations (e.g., [8,12,13]). Here, the membership functions applied are shown in Figure 1. The membership functions for M_T, M_{RH}, M_{CTT}, 3-h M_P and M_{vv} were adopted from [12], while the membership of cloud liquid water content (M_{CLWC}) by Belo-Pereira [13] was used instead of the Supercooled Liquid Water Content of [12], as it was not available in the COSMO model output. Additionally, it has been suggested that the use of CLWC in the icing forecast may reduce the false rates as supercooled cloud water is generally underestimated by the NWP models [8,13].

For the determination of the meteorological conditions favorable for icing formation and possible meteorological scenarios, the IPA used the definitions by [12] Specifically, 3 h total precipitation and convective and largescale snow forecasts were used to determine the precipitation types as rain (RA), snow (SN), freezing rain (FZRA) and ice pellets (IP) based on the model total precipitation and snow values combined with the model T and the algorithm defined CTT. The determination of all types was based on the classification by [17], as applied in [12]. Hence, situations of single-layer, non-precipitating clouds, single-layer, precipitating clouds (no freezing rain), multiple cloud layers and classical freezing rain structures were applied. Up to this point, an initial IPA was calculated depending on the meteorological situation determined, as the product of the effects of T, RH and CTT (where applied) and accumulative precipitation (AP), where applied.

Specifically for the effect of AP, if SN was forecasted and the temperature was below freezing, the effect was negative and the IPA was decreased, as the presence of ice crystals was expected to diminish the amount of supercooled liquid droplets, while the IPA was also controlled by the effects of T, RH and CTT (at cloud top). If liquid RA was present and the temperature was below freezing, the effect was added to the IPA. In the case of a classical FZRA structure, (in which FZRA occurs as snow melts in a warm layer and then in a layer below the cloud base at which T is below freezing and supercooled droplets exists), then the IPA below the estimated cloud base was controlled by T and boosted by the AP interest due to the potential presence of supercooled liquid water, while above the cloud base the situation was treated as a single cloud case [12].

Finally, the vertical velocity and cloud liquid water content effects on IPA were added. The first either added to or reduced the initial value, as upward motion (negative ω) lifts the air, which then cools and increases its RH, leading to a larger amount of supercooled droplets being formed at these levels. On the other hand, downward motion (positive ω) leads to cloud dissipation and reduces the formation of supercooled liquid water [7,12]

(Figure 1e), although in a newer study it is mentioned that close to the levels where in-flight icing is formed, ω is positive in over 50% of moderate events and almost 30% of severe events [16]; however, this remark has not been included in the present study. The inclusion of the cloud liquid water content effect in the IPA was expected to increase the predicted icing formation on the airframe as cloud liquid water droplets in temperatures below zero freeze on the exposed surfaces of an airplane during flight [13,18] and this is reflected in the M_{CLWC} membership function (Figure 1f).



(**a**) (**b**) (**c**)

(**d**) (**e**) (**f**)

Figure 1. The membership functions for (**a**) temperature; (**b**) cloud top temperature; (**c**) relative humidity; (**d**) 3haccumulative precipitation; (**e**) vertical velocity and (**f**) cloud liquid water content. Membership functions from (**a**–**e**) were adopted from [12], while membership function (**f**) was adopted from [13].

Hence, taking into account the previously mentioned remarks, the IPA included the calculation of an initial value of icing potential (IP_{init}), accounting for the influences of the different meteorological parameters T, RH, CTT (where it applied) and AP (dependent on the precipitation type) for the associated meteorological situation:

$$IP_{init} = M_T \times M_{RH}[\times M_{CTT}] \pm M_{AP}. \quad (1)$$

Equation (1) calculates IP_{init}, incorporating the influences of T, RH and CTT by multiplying the values of the related membership functions corresponding the values of temperature and relative humidity to the icing potential, while the membership function of CTT is taken into account only at the top of the cloud each time; for this reason, it was included in brackets in the equation. Depending on the type of the precipitation, i.e., RA, FZRA, SN or IP as described previously, the corresponding membership function was either added or subtracted from the product of the other membership functions (±signal use in Equation (1)). To this initial value IP_{init}, the effect of the vertical velocity and the cloud liquid water content was included. Following the description of the simplified forecast

Icing Potential Algorithm (SFIP) by [13], this work used also different weighting factors, W_{vv} and W_{CLWC}, respectively, to account for the effects of M_{vv} and M_{CLWC} in the form of five scenarios (S1 to S5), as shown in Table 1, and considered also IP_{init} as scenario S0. The values used were arbitrary and, in the absence of the PIREP database over the IFR of Greece, these values were applied in order to identify the sensitivity of the IPA on these meteorological parameters to the final value of the icing potential (IP):

$$IP = IP_{init} + W_{vv} \times M_{vv} + W_{CLWC} \times M_{CLWC}. \quad (2)$$

Hence, Equation (2) incorporates the effect of VV and CLWC by multiplying the related membership functions corresponding to their values with the chosen weight and adding their products to the initial IP value. It is noted that M_{vv} was either positive or negative for upward or downward motion, respectively, as shown in Figure 1e. The structure of the IPA is illustrated schematically as a flowchart in Figure 2.

Table 1. Scenarios applied for the contribution of vertical velocity and cloud liquid water content in the calculation of IP.

Scenario	W_{vv}	W_{CLWC}
S0	0	0
S1	0	1
S2	1	0
S3	0.25	0.75
S4	0.50	0.50
S5	0.75	0.25

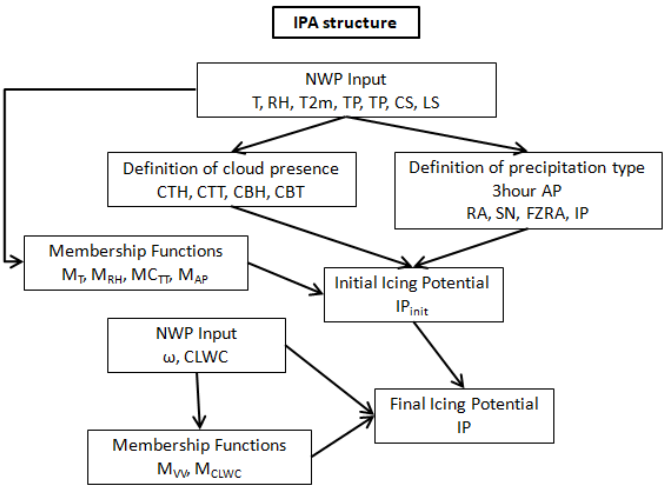


Figure 2. Flowchart of the IPA.

2.2. The NWP Model

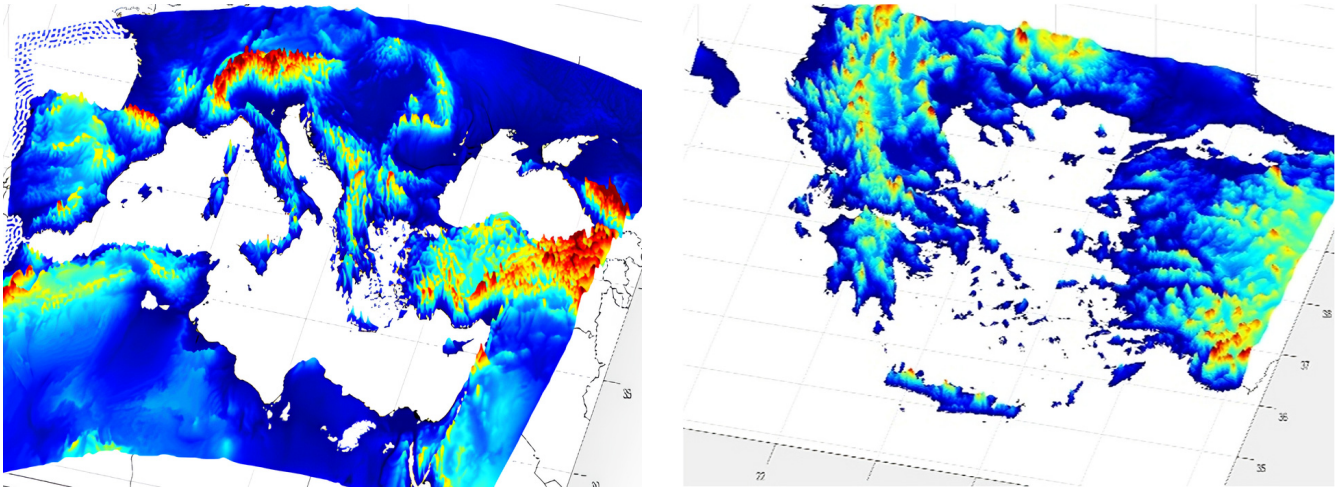
For providing forecasts for severe weather conditions, direct model output products are usually used from high-resolution Numerical Weather Prediction (NWP) systems. The COSMO-GR NWP model, which is used in this paper in order to apply and evaluate the recommended methodology, is a non-hydrostatic model developed within the framework of the COSMO Consortium (Consortium for Small-scale Modeling) [19,20]. The COSMO model was developed to provide high spatial resolution forecasts and serves as a versatile tool for numerous research applications.

Recent improvements to the COSMO model at the convective scale have made it capable of providing enhanced forecasts regarding the location, timing and severity of deep convection, aiming to improve precipitation forecasts during the summer compared to lower-resolution NWP models that use parameterized for deep convection [21]. To achieve

this goal, a new dynamic core was developed, utilizing a reliable Runge–Kutta solver. Additionally, several extensions and improvements to the physical parameterizations were necessary.

At the convective scale, optimal parameterization of the boundary layer (BL) is crucial for successful forecasts, especially in the initiation process of deep convection. Reducing the asymptotic mixing height and assumptions related to cloudiness in the parameterization of the BL scheme at the subgrid scale leads to significant improvements in the numerical representation of physical processes. The microphysics of deep convection clouds is more complex than that of stratiform clouds and requires more sophisticated parameterization. As a result, the cumulative 12 h precipitation remains largely unaffected by changes in cloud microphysics, while cases where convection is triggered by existing cells as secondary convection are more sensitive to microphysical assumptions. Evaluations conducted on the high-spatial resolution version of the model at the research level indicate that the COSMO model at convective resolution has improved performance.

For the current study, the model was implemented with two one-way nested domains, COSMO-GR1, the convective-scale-resolving version with a horizontal resolution of 0.01° (approximately 1 km), initialized from COSMO-GR4 with a resolution of 0.04° (approximately 4 km) with parameterized convection. The coarse domain covered the broader Mediterranean region, while the inner domain encompassed the greater geographical area of Greece. In terms of the vertical axis, 80 vertical levels were utilized, extending up to 30 hPa, covering most of the atmosphere, with increased resolution near the boundary layer, starting from a few meters above the surface (20.0 m) using a terrain-following approach [22]. The ECMWF IFS operational analyses served as the initial and lateral boundary conditions for the coarse domain. For the present case study application, the model was initialized at 12:00 UTC on 11 March 2019 and run for a 48 h forecast period. Model output was available at hourly intervals. The integration areas of the models are shown in Figure 3.



(**a**) (**b**)

Figure 3. Integration grid of the (**a**) COSMO=GR4 (4 km grid spacing) and (**b**) COSMO-GR1 (1 km grid spacing) models, showing the orography from low heights (blue color) to large heights (red color).

2.3. Observations

Remote sensing observations as well as point observations at specific airports were used to discuss the meteorological conditions that occurred during the study period and at the same time to qualitatively evaluate the results of IPA.

2.3.1. Satellite Data

As an attempt to identify icing conditions in the atmosphere, EUMETSAT's Meteosat Second Generation satellite data were used. The Spinning Enhanced Visible and Infrared

Imager (SEVIRI) instrument has multiple spectral channels, including visible, near-infrared and infrared wavelengths. The direct brightness temperature product was not sufficiently definitive for determining in-flight icing conditions, thus postprocessed derived parameters were used to enhance this study's findings. These are the cloud phase and the cloud top height products.

The cloud phase product provides critical information about the physical state of clouds [23]. The primary goal of this product is to distinguish between different types of clouds, which can significantly impact weather forecasting and aviation safety. The cloud phase can indicate ice clouds, water clouds or multi-layer clouds. Ice Clouds are composed primarily of ice crystals and are typically found at higher altitudes in subfreezing environment. Water Clouds consist mainly of liquid water droplets and are usually located at lower altitudes where temperatures are above freezing. Multi-layer Clouds contain both ice crystals and liquid water droplets, indicating the presence of different cloud layers with varying thermal and microphysical properties.

The cloud top height (CTH) product provides information on the altitude of the uppermost layer of clouds. The retrieval of cloud top height involves several steps. The primary method uses infrared (IR) radiances to determine the temperature at the cloud top. Cloud top temperature data from EUMETSAT's NWP SAF were used, as they serve an intermediate step for cloud top height calculation. This temperature was then converted to height using atmospheric temperature profiles from NWP models. A key part of the algorithm was the use of the EUMETSAT Numerical Weather Prediction Satellite Application Facility (NWP SAF) (https://nwp-saf.eumetsat.int/site, accessed on 20 December 2023), which provides accurate temperature profiles necessary for the conversion of radiances to cloud top heights.

2.3.2. Radar Data

For the needs of the current study, data from the Hellenic National Meteorological Service (HNMS) weather radar network were used, which provides near real-time spatio-temporal monitoring of the atmosphere. Specifically, data from Larissa S-band (2.7 GHz) Doppler weather radar located at latitude 39.6446° N and longitude 22.4603° E were retrieved. The radars provide twelve elevation Plan Position Indicator (PPI) scans, with a horizontal resolution of 400 m. These remote sensing observations were crucial for identifying regions of intense convection and therefore, potential icing conditions.

2.3.3. METARs

In addition to the remote sensing observations that included information for the structure and the characteristics of the atmosphere from above, surface stations METAR (Meteorological Airport Report) data were employed to facilitate the comparison with the presence of clouds or certain meteorological phenomena in the vicinity of a station that may be associated with icing presence.

As METARs represent an accurate report of the weather conditions at the surface of a fixed location and at a temporally continuous interval, they were used to determine icing events and evaluate the predictions of aircraft icing conditions (e.g., [24]). For example, when freezing rain or freezing drizzle was recorded, an SWD event was more likely to exist between the surface and the lowest cloud base of at least "broken" coverage (i.e., 5–7/8 sky coverage). Then the ceiling value was used to estimate the depth of the observed SWD layer [25].

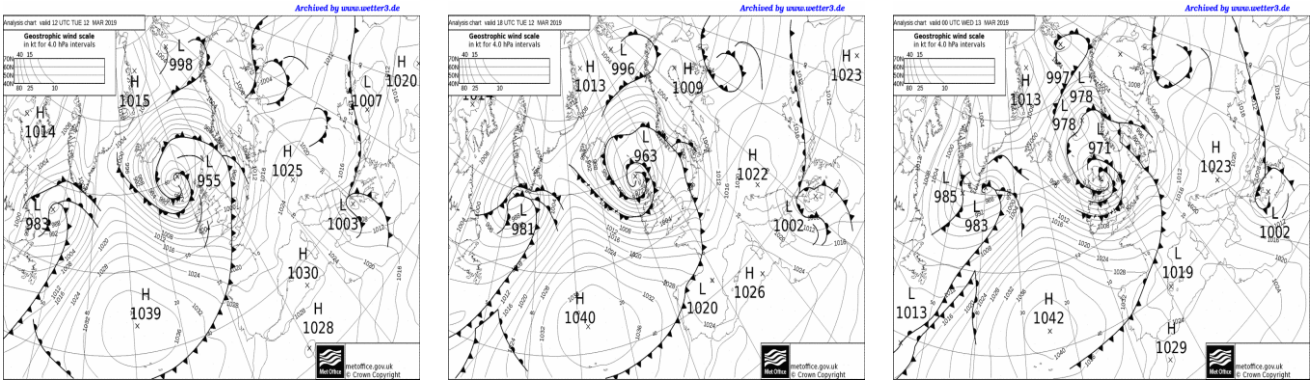
In our case study, METAR data were used to extract information on the precipitation and cloud type, the cloud base height and its sky coverage in combination with the observed temperature values. Specifically, half-hourly observations from Nea Aghialos (LGBL) airport (39.2217° N, 22.7690° E) at the center of continental Greece were retrieved for the meteorological conditions and analyzed below.

3. Results

As already mentioned, this is the first application of the IPA over Greece. At the moment, the IPA is applied for research purposes. The IPA methodology application leads to output information that includes (a) existence of single or multi-layer clouds, (b) cloud base and top heights, (c) air temperature at the corresponding cloud base and top heights, and finally (d) IP fields resulting from the various scenarios every 3 h at 12 different flight levels from 1000 to 40,000 ft (resulting from the corresponding model levels from 305 m up to 12,192 m) and at the horizontal resolution of the COSMO-GR NWP model inner domain (1 km).

3.1. Case Study

The synoptic meteorological case chosen to be studied with the IPA was that of an intense depression over Greece. The 12 March 2019 was characterized by an intense low-pressure system moving over Greece from the northwest at 00UTC, followed by an occlusion that was also associated with a cold and a warm front. These conditions influenced the weather throughout the country from 12UTC and until after the 13 March 12UTC.Figure 4 shows the UK Meteorological Office (UKMO) analysis chart from 12 March 2019 12UTC to 13 March 2019 00UTC every 6 h. Specifically, the depression had its center located in the marine area northwest of Greece with the pressure at 1003 HPa at 12UTC, then it slightly deepened (1002 HPa) and moved to the continental Greece at 18UTC and shifted slowly eastwards 6 h later. The occlusion mainly affected the maritime area west and northwest of Greece until 12 March 2019 18UTC and then, as the center moved eastwards, influenced a large part of the central and south Greek territory. The associated cold front initially spanned over west Greece and then the largest part of Greece, expanding from the north–central Greece to the south at 18UTC and 6 h later was shifted to the east, while the warm front mainly affected the north–northeast part of Greece at all times. This synoptic pattern was explicitly selected because it is dynamically significant in terms of aviation safety as the meteorological phenomena associated with it are embedded convective clouds, thunderstorms, turbulence and icing conditions. Specifically, in the context of this work, the ascent of the air above a low-pressure system is usually associated with the development of convective clouds that are dependent on the air temperature and are characterized by the presence of supercooled liquid water and crystals at specific levels, constituents that, as already discussed, are important for in-flight icing formation. Additionally, the fronts that accompany a depression may be followed by unstable conditions in the warm air, enhancing the possibility for the formation of clouds with large vertical extents, and may be expected to include significant updrafts and large supercooled water droplets and thus potential conditions for icing formation.



(**a**) (**b**) (**c**)

Figure 4. UKMO analysis charts: (**a**) 12 March 2019 12UTC; (**b**) 12 March 2019 18UTC; and (**c**) 13 March 2019 00UTC (from https://www1.wetter3.de/archiv_ukmet_dt.html, accessed on 30 September 2022).

In a case of precipitation formation by clouds developing on a frontal surface, thunderstorms would be expected to develop from convective clouds, while in the case of stratiform clouds, the presence of the cold air below could lead to the formation of precipitation types that are associated with the presence of supercooled droplets, such as freezing rain, although the METAR observations did not reveal such case on the surface of the selected airdrome, as discussed in Section 4.

Figure 5 shows the COSMO-GR predicted temperature and relative humidity (RH) levels at 20,000 ft (approximately 500 mb) on 12 March at 12UTC, presenting the forecasted prevailing conditions at the upper level. It was suggested that there was a cold intrusion with temperatures below −32 °C in the northwest part of Greece. At the same time, large values of the predicted RH (more than 60%) were extended over the largest part of the country. In the same figure, the 0 °C isotherm predicted by the NWP model is also shown at the particular time. It showcases that subfreezing areas existed at lower levels (below 3000 ft) in the vicinity of the occlusion and behind the cold front (below 4000 ft) and in front the warm front in northeast Greece (below 2000 ft), as expected, and over 6000 ft in the rest of the regions. Additionally, the 24 h precipitation amount based on IMERG data [26] is shown in Figure 6. Precipitation existed over the whole country, with several areas covered by large amounts, such as Central Continental Greece around the Nea Aghialos airport (LGBL) and the Aegean Sea located at the east.

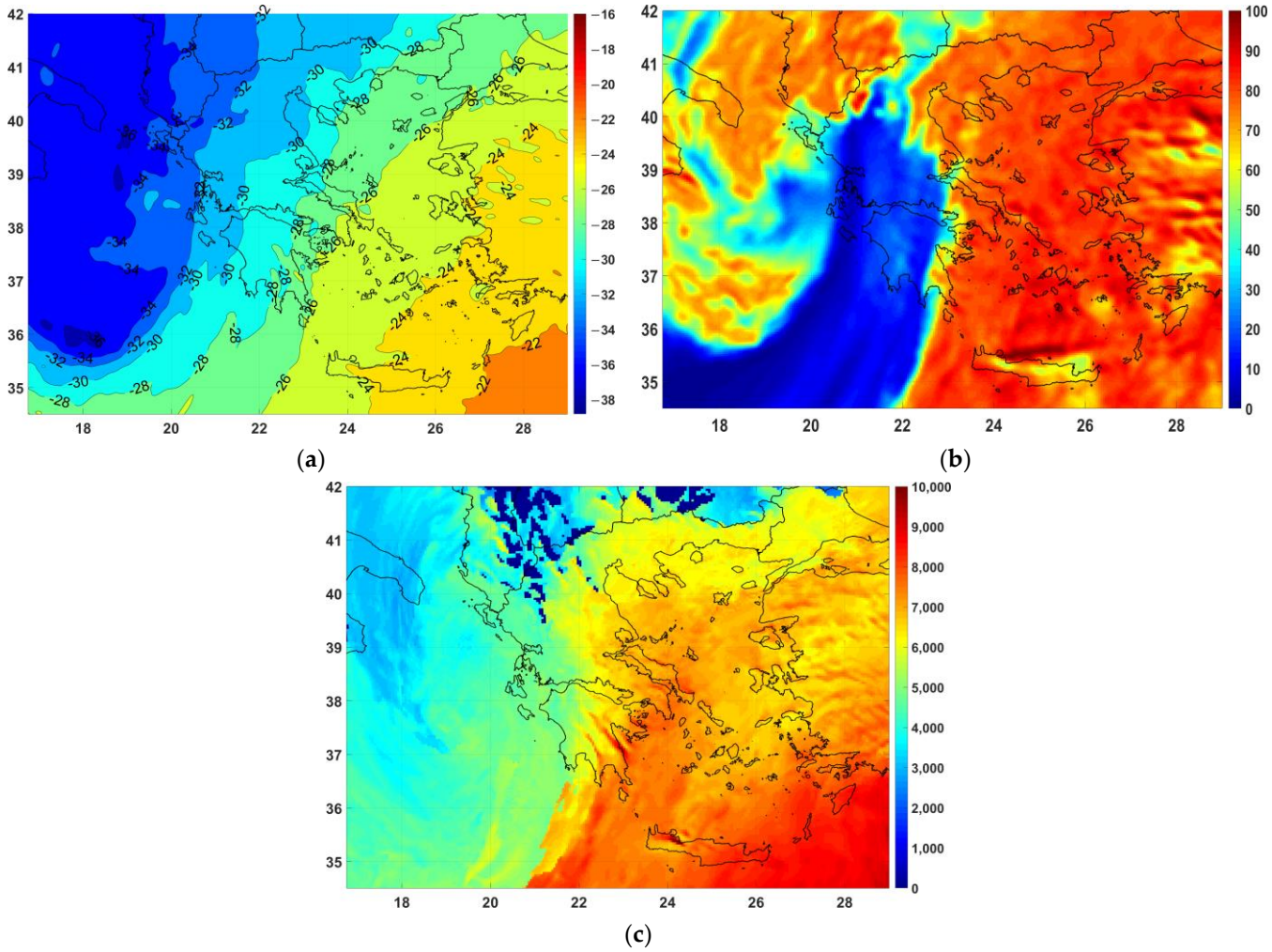


Figure 5. COSMO-GR predictions of (**a**) temperature and (**b**) relative humidity at 20,000 ft and (**c**) the 0 °C isotherm height on 12 March 2019 12UTC.

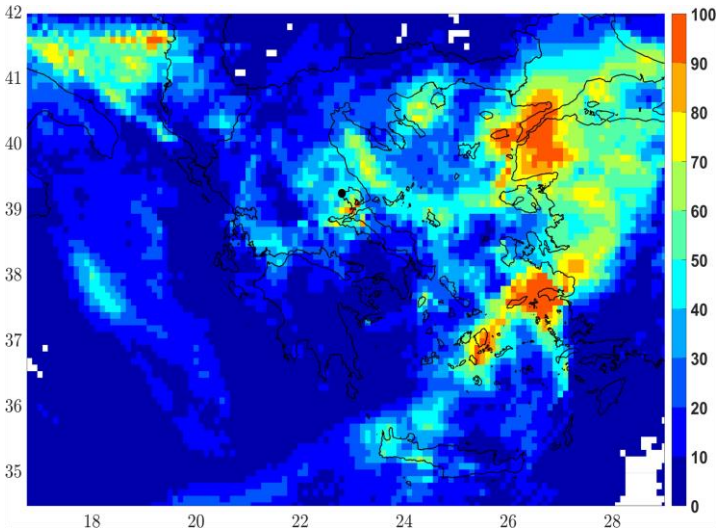
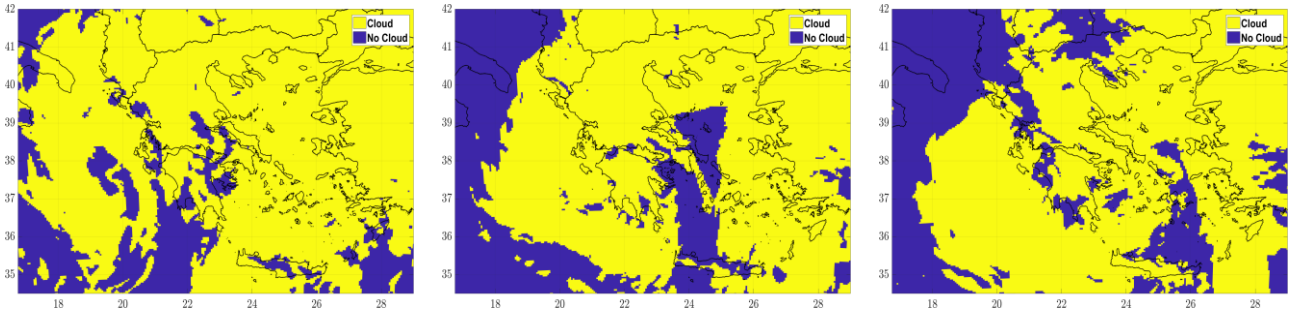


Figure 6. IMERG 24 h precipitation on 12 March 2019. LGBL (Nea Aghialos) airport is shown with the black dot at the central continental Greece.

3.2. Cloud Presence Estimation with IPA

3.2.1. Cloud Mask

The IPA first defined the presence of one or multiple clouds as already discussed. Here, the estimated cloud mask is shown on 12 March 2019 at 12UTC and 18UTC and on 13 March 2019 at 00UTC (Figure 7). Comparing these graphs with the corresponding UKMO analysis charts (Figure 4), it seems that the estimated cloud mask was in accordance with the location of the low-pressure system and the associated fronts, while the large horizontal extent of the clouds suggested potential precipitation events, as the IMERG data indicated (Figure 6).



(**a**) (**b**) (**c**)

Figure 7. Cloud mask field estimated by the IPA: (**a**) 12 March 2019 12UTC; (**b**) 12 March 2019 18UTC; and (**c**) 13 March 2019 00UTC.

3.2.2. Cloud Base and Top Heights

In addition, the IPA estimated the height of the base (Figure 8) as well as the height of the top of the clouds (single or multiple) as well as their corresponding temperatures (Figure 9). The clouds over the area of Greece seemed to expand from less than 5000 ft, in certain areas where the cold front was expected to be present, up to 40,000 ft, indicating deep convectivity in those regions, if single clouds are present, with their temperature ranging from positive values or close to 0 °C to −30 °C to −40 °C. Specifically, the cloud base temperature exhibited positive values mainly at the location of the warm section between the cold and the warm fronts, as shown in Figure 9. The cloud top temperature was generally negative, apart from the areas where the height of the cloud top was small and the clouds forecasted extended to less than 10,000 ft (Figure 8). The expected type of the clouds is discussed in the following sections.

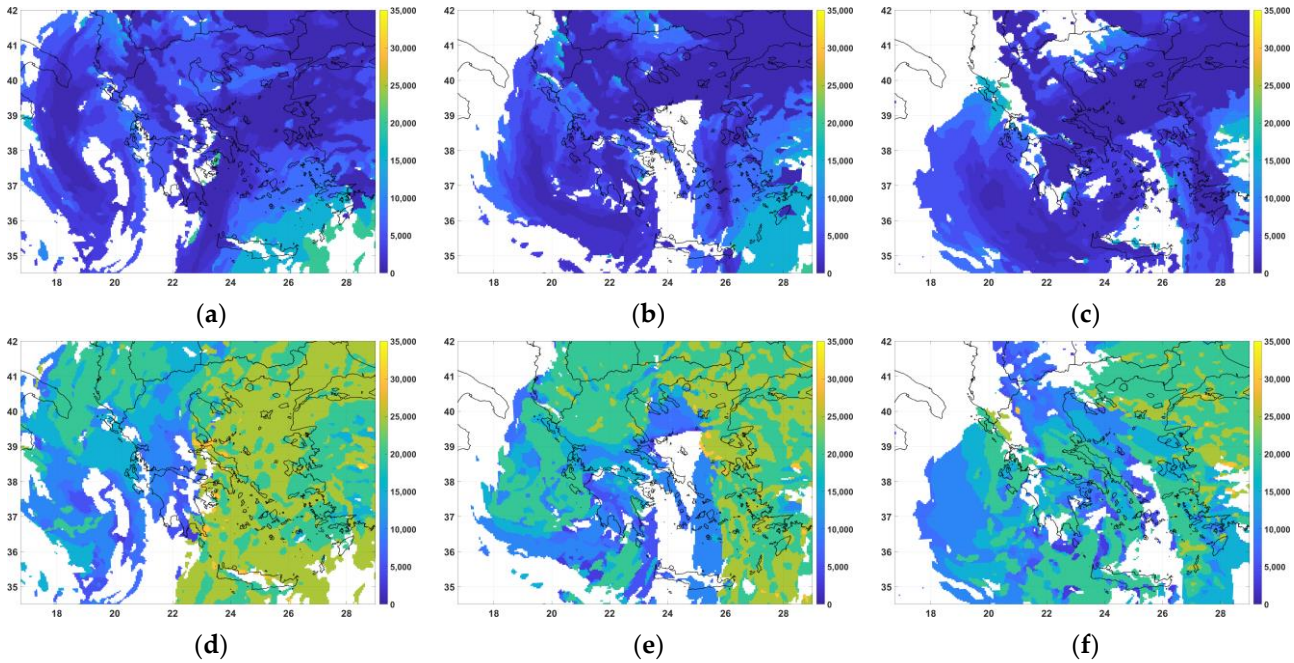


Figure 8. Cloud base height: (**a**) 12 March 2019 12UTC; (**b**) 12 March 2019 18UTC; (**c**) 13 March 2019 00UTC, and Cloud top height on: (**d**) 12 March 2019 12UTC; (**e**) 12 March 2019 18UTC; and (**f**) 13 March 2019 00UTC, as estimated by the IPA.

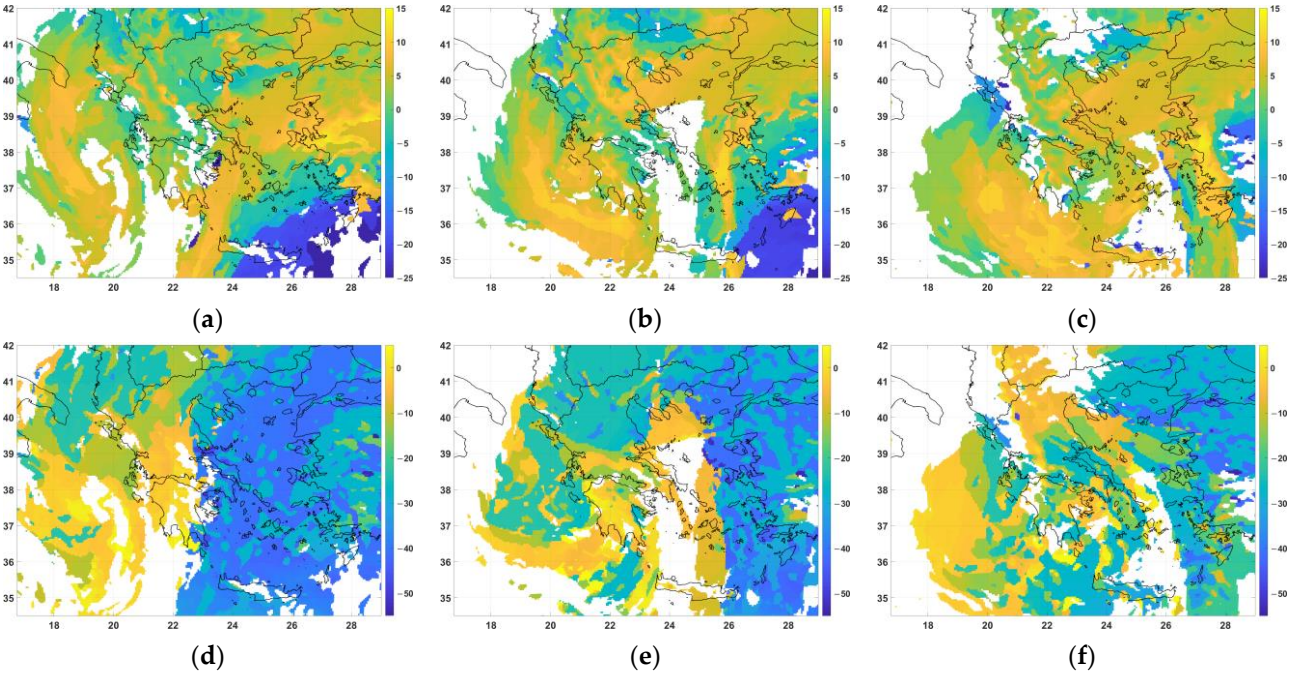


Figure 9. Cloud base temperature: (**a**) 12 March 201912UTC; (**b**) 12 March 2019 18UTC; and (**c**) 13 March 2019 00UTC. Cloud top temperature: (**d**) 12 March 2019 12UTC; (**e**) 12 March 2019 18UTC; and (**f**) 13 March 2019 00UTC, as estimated by the IPA.

3.3. Icing Potential Forecast Scenarios

Here, the icing potential estimations based on IP_{init} (hereafter referred to as IP_{S0}) and the use of the effects of vertical velocity and cloud liquid water content using different weights vertically at different flight levels are shown for 12 March 2019 at 12 UTC. Figure 10 illustrates the values of IP_{S0} as a percentage of icing presence. It is evident that icingfor-

mation was estimated to be significant from the lower levels of 1000 ft and 3000 ft, while over 5000 ft and up to 10,000 ft icing covered the largest area over Greece, with percentages of at least 70%, while above 15,000 ft IP_{S0} started decreasing over several regions. At 25,000 ft IP_{S0} was estimated to be significant, primarily over the Aegean Sea, whereas it fell below 10% over continental Greece, and over Crete and the Eastern Mediterranean it was reduced to values less than 60%. Finally, at heights from 30,000 ft and higher, IPS0was no longer important.

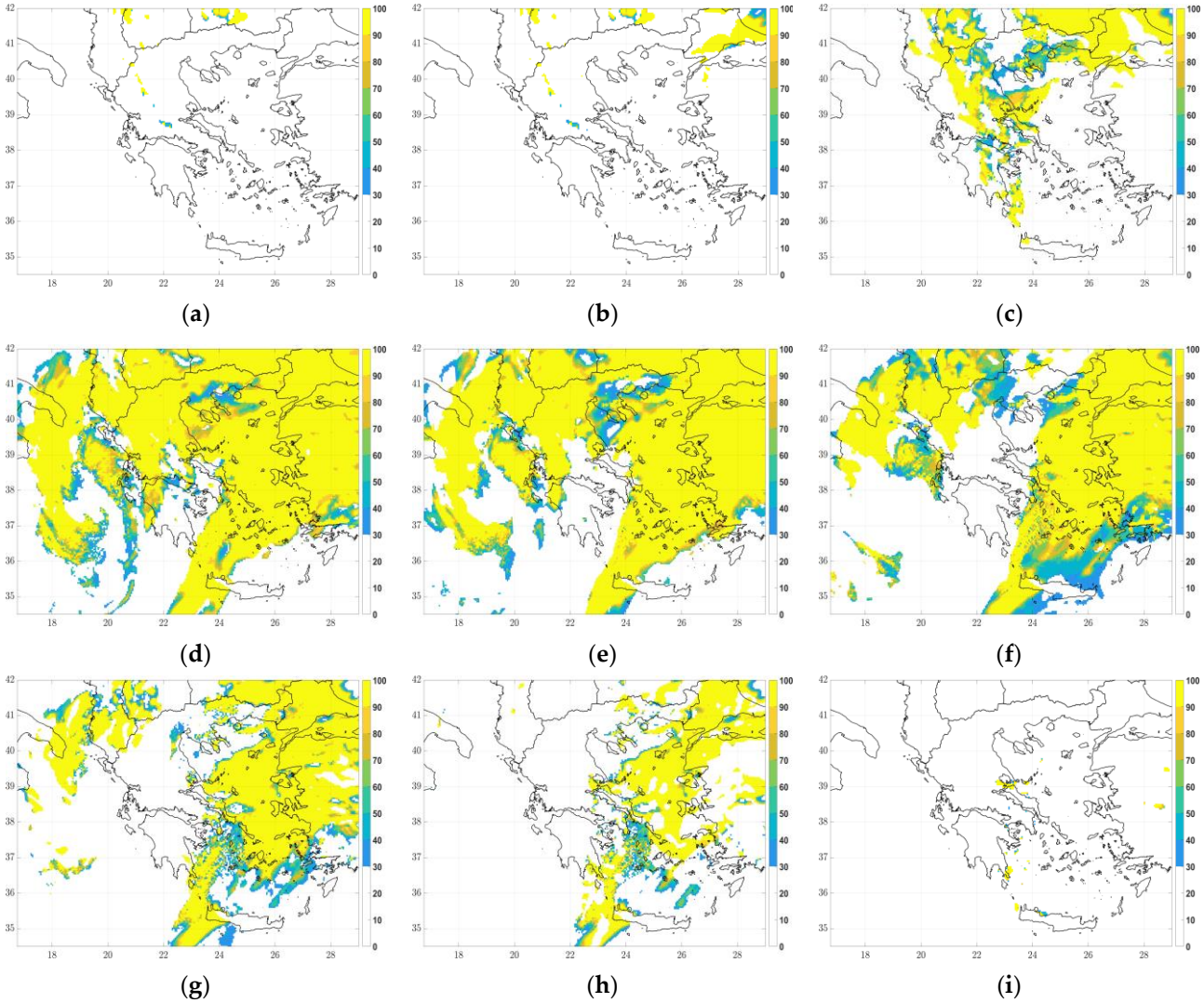


Figure 10. IP_{S0} estimated on 12 March 2019 12UTC at different flight levels: (**a**) 1000 ft; (**b**) 3000 ft; (**c**) 5000 ft; (**d**) 8000 ft; (**e**) 10,000 ft; (**f**) 15,000 ft; (**g**) 20,000 ft; (**h**) 25,000 ft; and (**i**) 30,000 ft.

The various scenarios exploring the different weighting factors of M_{CLWC} and M_{vv} effects are presented here in terms of differences from the initial values of icing potential:

$$\text{Diff} = IP_{S0} - IP_{S1,2,3,4,5}, \quad (3)$$

where $IP_{S1,2,3,4,5}$ is the resulted value calculated from Equation (2) after using each of the scenarios S1 to S5 described in Table 1. The resulting values suggested that the differences (positive indicating higher values of IP_{S0} or negative, i.e., lower values of IP_{S0}) were significant over Greece at flight levels between 5000 ft and 25,000 ft. The scenarios where M_{vv} was taken into account had larger impacts in the resulting value than the effect of M_{CLWC} itself. When M_{vv} alone was considered (IP_{S2} in Figure 11) it either boosted (negative

values) or decreased IP (positive values) at all flight levels where IP was significant, while it is interesting to notice that the boosting attribution was almost the only effect at the level of 20,000 ft and 25,000 ft suggesting that there was mainly upward motion of the air at those particular cloud areas, indicating possibly convective conditions in those regions, appearing at all forecasting times (here only the 12UTC on 12 March 2019 is shown).

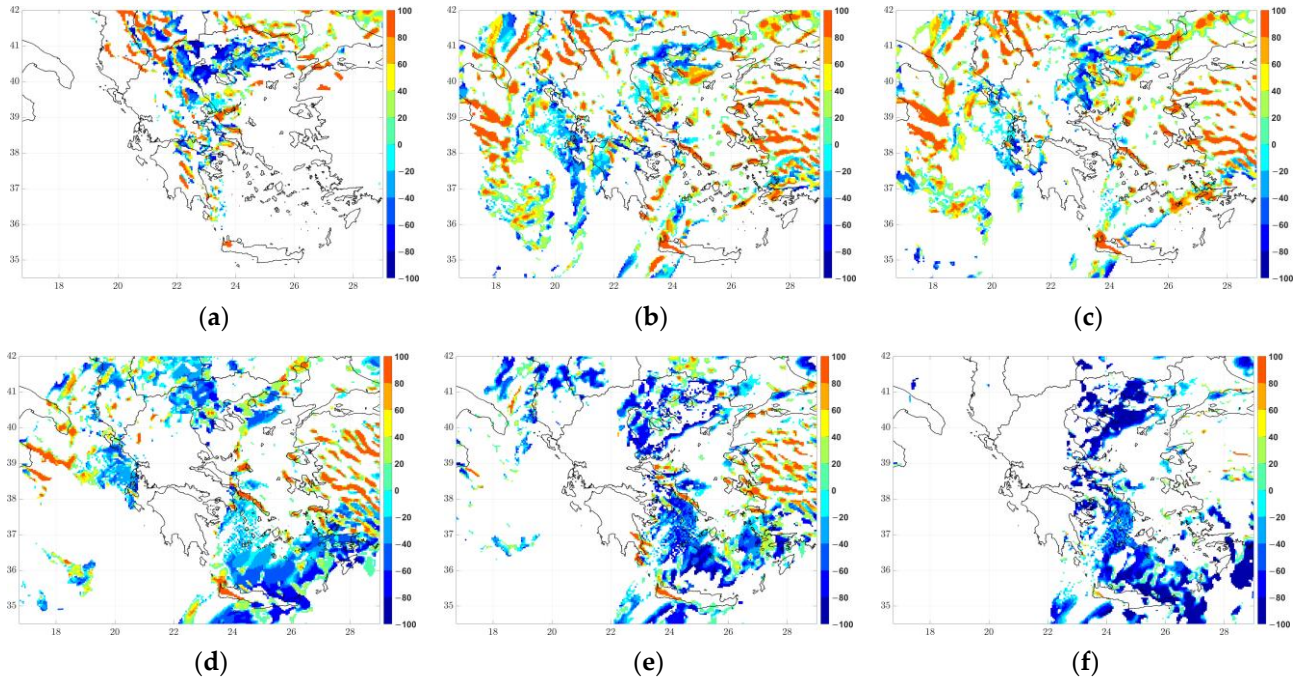


Figure 11. Difference between IP_{S0} and IP_{S2} as calculated on 12 March 2019 12UTC at different flight levels: (**a**) 5000 ft; (**b**) 8000 ft; (**c**) 10,000 ft; (**d**) 15,000 ft; (**e**) 20,000 ft; and (**f**) 25,000 ft.

On the other hand, when the effect of vertical velocity was absent and the only additional effect was the one that resulted from cloud liquid water content (IP_{S1}) it seems that the resulted IP value was not greatly affected by the impact of M_{CLWC} alone at all forecasting times, showcasing only a minor impact at certain locations, generally different at each forecast time, with a positive impact of M_{CLWC}; for this reason results of IP_{S1} are not further discussed.

The resulting IPs from the other three scenarios ($IP_{S3,4,5}$) were mainly influenced to be greater or lesser by the M_{vv} depending on the weight given to the membership function. Therefore, the IPA is sensitive, apart from its initial contributions (IP_{S0}), also on the vertical velocity. Figure 12 shows selected levels (5000 ft; 10,000 ft; 15,000 ft) for the three remaining scenarios ($IP_{S3,4,5}$), showcasing that the sensitivity of IP from M_{vv} increased with increased W_{vv}.

To discuss the sensitivity of the IPA on vertical velocity, it is necessary to consider that, based on the synoptic picture of the case study, it is expected that the presence of the low-pressure system with the associated three fronts may provide convective conditions that in regions is expected to be strong. This would imply, in unstable conditions, the presence of deep convective clouds (cumulonimbus-CB or Towering Cumulus-TCU) or altocumulus (AC) as middle-level clouds or cirrocumulus (CC) as high-level clouds on the frontal surfaces. SWDs are commonly present in CB, TCU, AC and CC, depending on the air temperature, with updrafts generally occurring within and below them (except for CB, where both updrafts and downdrafts exist). Hence, this explains that in this case study, vertical velocity was meteorologically important for specific cloud-types and icing formation.

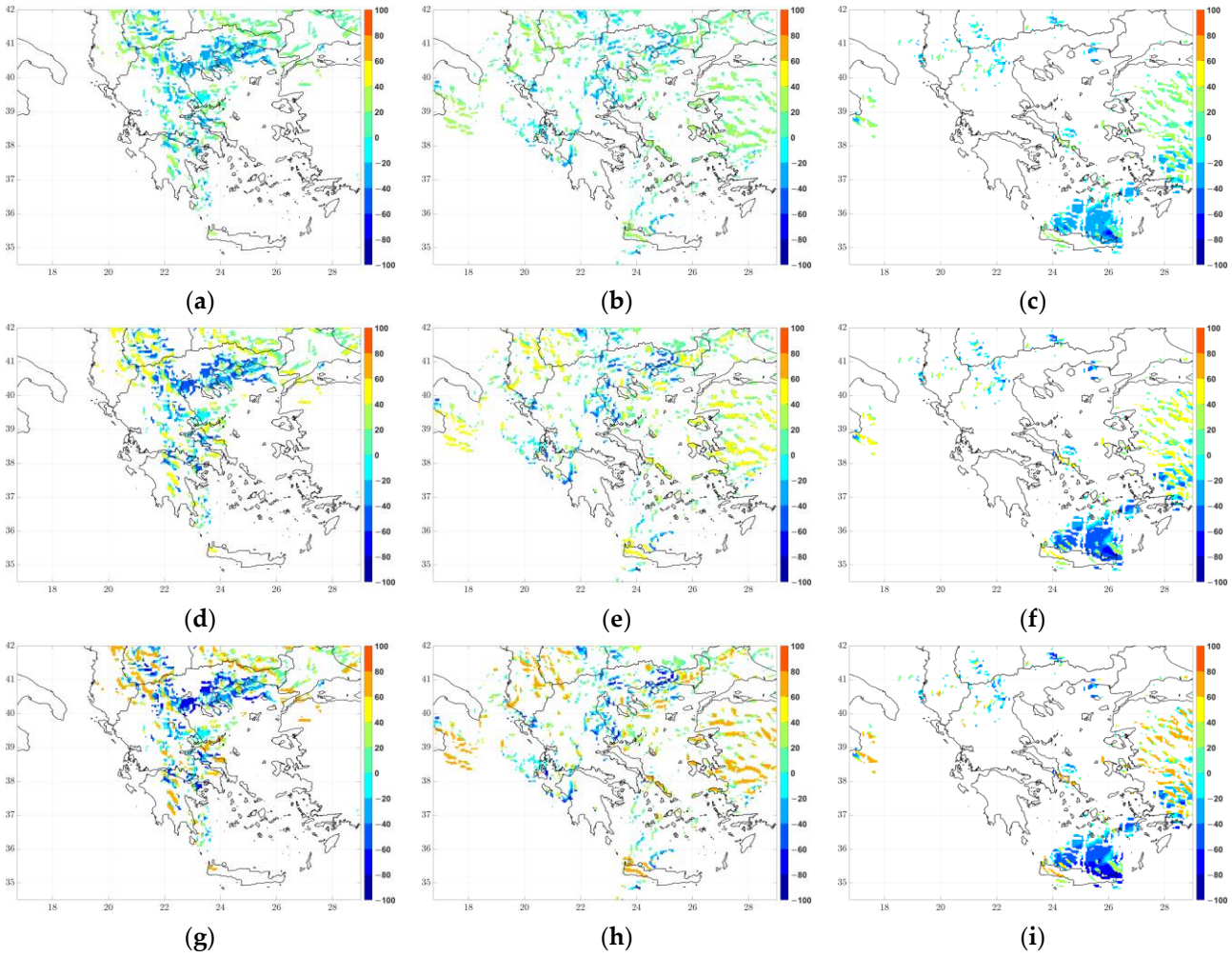


Figure 12. Difference between IP_{S0} and IP_{S3} at (**a**) 5000 ft; (**b**) 10,000 ft; (**c**) 15,000 ft; between IP_{S0} and IP_{S4} at (**d**) 5000 ft; (**e**) 10,000 ft; (**f**) 15,000 ft; and between IP_{S0} and IP_{S5} at (**g**) 5000 ft; (**h**) 10,000 ft; and (**i**) 15,000 ft as calculated on 12 March 2019 12UTC.

4. Qualitative Evaluation of the Algorithm over Greece

It has been previously mentioned that there is no available PIREP database for the FIR (Flight Information Region) of Greece to evaluate the IP scenarios of this study directly by using the conventional statistical methods for evaluating dichotomic events (yes/no icing on a certain level) as Probability of Detection (POD), False Alarm Rate (FAR), etc. The statistical analysis conducted by [13] on the Simplified Forecast Icing Potential (SFIP) algorithm, utilizing weights for different membership functions, demonstrated that the $SFIP_0$ scenario with weights for M_{vv} 0.2 and M_{CLWC} 0.45 exhibited the highest overall performance and $SFIP_3$ with weights for M_{vv} 0.4 and M_{CLWC} 0.0 were the second best for certain statistical scores and icing intensity categories. Following a similar approach in this study, although it does not directly employ the same technique as SFIP, as in IPA, M_{RH} was considered together with M_T and M_{AP} for various meteorological situations within S0; we may assume that those scenarios partially correspond to our IP_{S3} and IP_{S2}, respectively. Additionally, our results indicated differences that were primarily attributed to the effect of vertical velocity. Therefore, scenarios S2 and S3, which include the highest weight of M_{vv} and the lowest weight of M_{CLWC}, will be discussed alongside scenario S0, in which M_{vv} and M_{CLWC} were absent.

The use of remote sensing products for detecting icing is generally applied in the last decades for nowcasting purposes. Nevertheless, it still remains in a relatively developing stage of research as remote sensing is not designed to detect directly icing and is used

mainly in combination with NWP results and/or surface observations to be analyzed and produce information on the location and the intensity of icing (e.g., [2,7,10,15,16,27–29]).

Here, in the absence of other resources and databases over Greece, remote sensing data were used not only ancillary to the IPA results, but also to provide some rate of qualitative evaluation of the algorithm. The IPA was based initially on the estimation and identification of clouds and their properties using COSMO prognostic fields. Therefore, firstly, we shall discuss the performance of the algorithm with respect to the available satellite and radar observations using them for comparison. Further, available METARs from selected airport are used to enhance the discussion.

4.1. Comparison with Satellite Observations

The satellite products used for comparison were the cloud top height as well as the cloud phase. Cloud top height (CTH) and cloud phase (CP) satellite products were retrieved for the forecast hours of the IPA output, which covers the period from 1200 UTC on 11 March 2019 to 1200 UTC on 13 March 2019. The IPA grid, which is the COSMO-GR model grid (rotated latitude and longitude), was interpolated to the satellite data grid to facilitate a direct comparison. Geostationary satellite projection with a resolution of 3 km $\times$ 3 km, was selected as a reference of the satellite data grid for evaluation. The IPA output was interpolated to the reference grid using the nearest neighbor method in MATLAB version 9.14 software. This method employs triangulation-based nearest neighbor interpolation, supporting 2-D interpolation. Cells without clouds of the IPA output were assigned a value of -999. The re-gridding procedure was applied both to the CTH and CP satellite products.

The IPA forecasts were compared directly to the water and ice clouds using a Boolean expression of yes or no, given that IP was calculated at specific heights. Since the CP product was calculated using the cloud tops, an adjustment was made for comparison. The IP was calculated as the maximum value at each atmospheric column of the vs. Each run included outputs at 12 vertical levels at specific heights starting from 305 m (=1000 ft), having the maximum value derived from all vertical levels. The CTH derived from IPA was compared to the corresponding satellite CTH estimations. The IPA output was set to provide values in 500-foot increments, initially derived in meters and subsequently converted to feet. A mathematical conversion of the 500-foot increments was applied to the satellite CTH data for a direct comparison.

Figure 13 illustrates (at the top) maps of the cloud top height, as observed by the satellite, and (at the bottom) the corresponding height resulting from the IPA on 12 March 2019 at 12UTC and 18UTC and on 13 March 2019 at 00UTC. At first glance, it was shown that the height of the cloud tops was generally underestimated by the algorithm (by at least 5000 ft) at most of the locations, although there was a similarity in the presence of the clouds and the general cloud mask, indicating the accordance with the low-pressure system and the associated fronts captured by the IPA, as already discussed. In general, the difference between satellite and the IPA CTH may lay in the fact that these two datasets are not numerically equivalent, having different horizontal resolutions. They were forced to be fitted in the same grid with interpolation and they both include possible errors in calculating CTH; the satellite CTH involves calculations through the temperature values estimated by the measured radiance and IPA values involve possible errors in the NWP temperature and relative humidity forecasts. Despite those differences, from the icing perspective, it was found that at heights generally greater than 30,000 ft, icing formation is not significant due to the reduced presence of SWDs, hence the underestimation of the height by the IPA compared to the satellite CTH was not as important as identifying the location of the clouds.

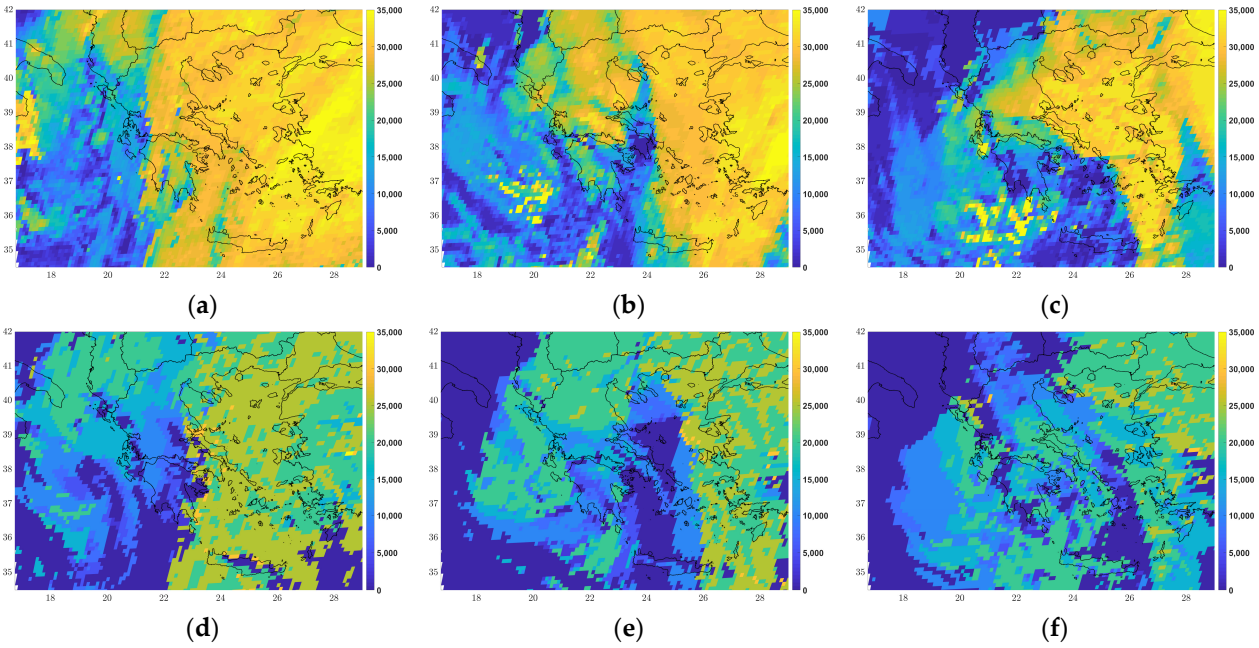


Figure 13. Cloud top heightfields as observed by the satellite (top): (**a**) 12 March 2019 12UTC; (**b**) 12 March 2019 18UTC; (**c**) 13 March 2019 00UTC and calculated by IPA (bottom) on: (**d**) 12 March 2019 12UTC; (**e**) 12 March 2019 18UTC; and (**f**) 13 March 2019 00UTC.

The optimal cloud analysis product for cloud phase was retrieved at 12UTC and 18UTC on 12 March 2019 and at 00UTC on 13 March 2019 and compared with the corresponding fields of IP_{S0}, IP_{S2} and IP_{S3} (Figures 14–16, respectively) over Greece. The satellite CP fields indicated single-layer water clouds (code 111-dark blue color), single-layer ice clouds (code 112-yellow) and multi-layer clouds (code 113-light blue). At the same time, the maximum IP fields were illustrated using threshold values similar to those generally used for identifying the severity of icing, namely for IP < 42.5% corresponding to "none-light icing", 42.5% < IP < 75% corresponding to "moderate icing" and IP > 75% associated with "severe icing" [30].

Based on the satellite images it was illustrated that water single-layered and multi-layer clouds were present at all three times, with multi-layer clouds predominating generally the areas affected by the fronts and the warm sector between the cold and the warm fronts. Hence, both ice and water clouds seemed to exist with the water clouds that were expected to include also supercooled liquid water as temperatures were below 0 °C, especially behind the cold front and within the subfreezing areas.

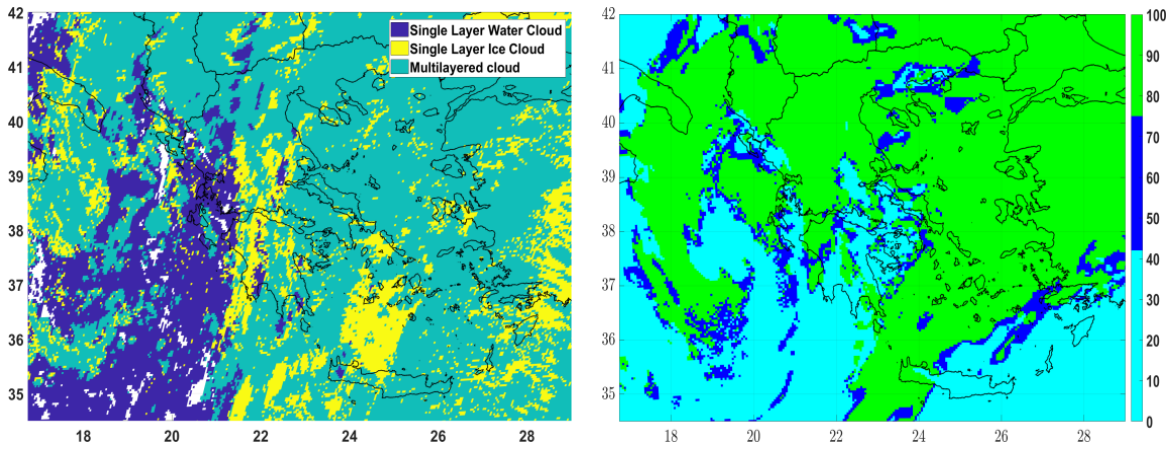


Figure 14. *Cont.*

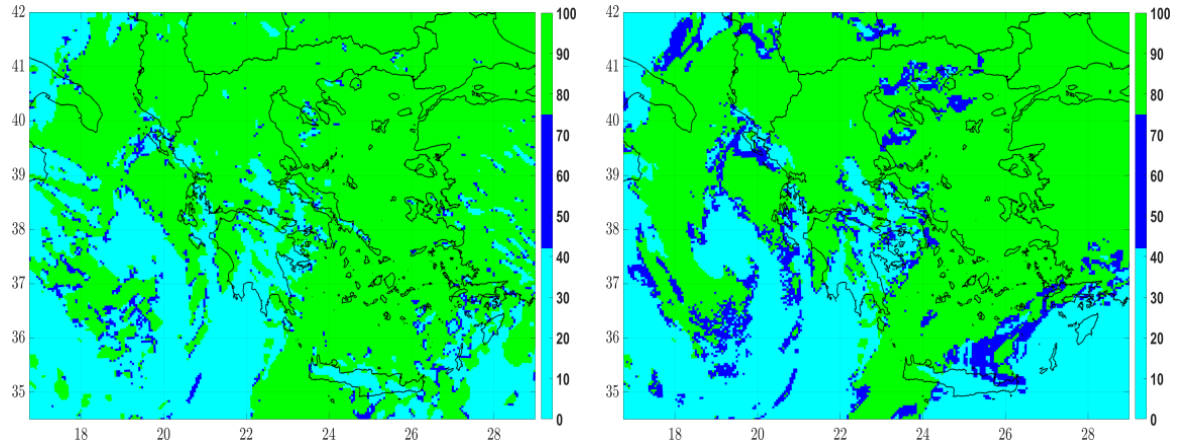


Figure 14. Comparison of (**a**) satellite cloud phase fields, with the maximum icing severity fields corresponding to "none-light" (cyan), "moderate" (blue) and "severe" (light green) for (**b**) IP_{S0}; (**c**) IP_{S2}; and (**d**) IP_{S3} on 12 March 2019 12UTC.

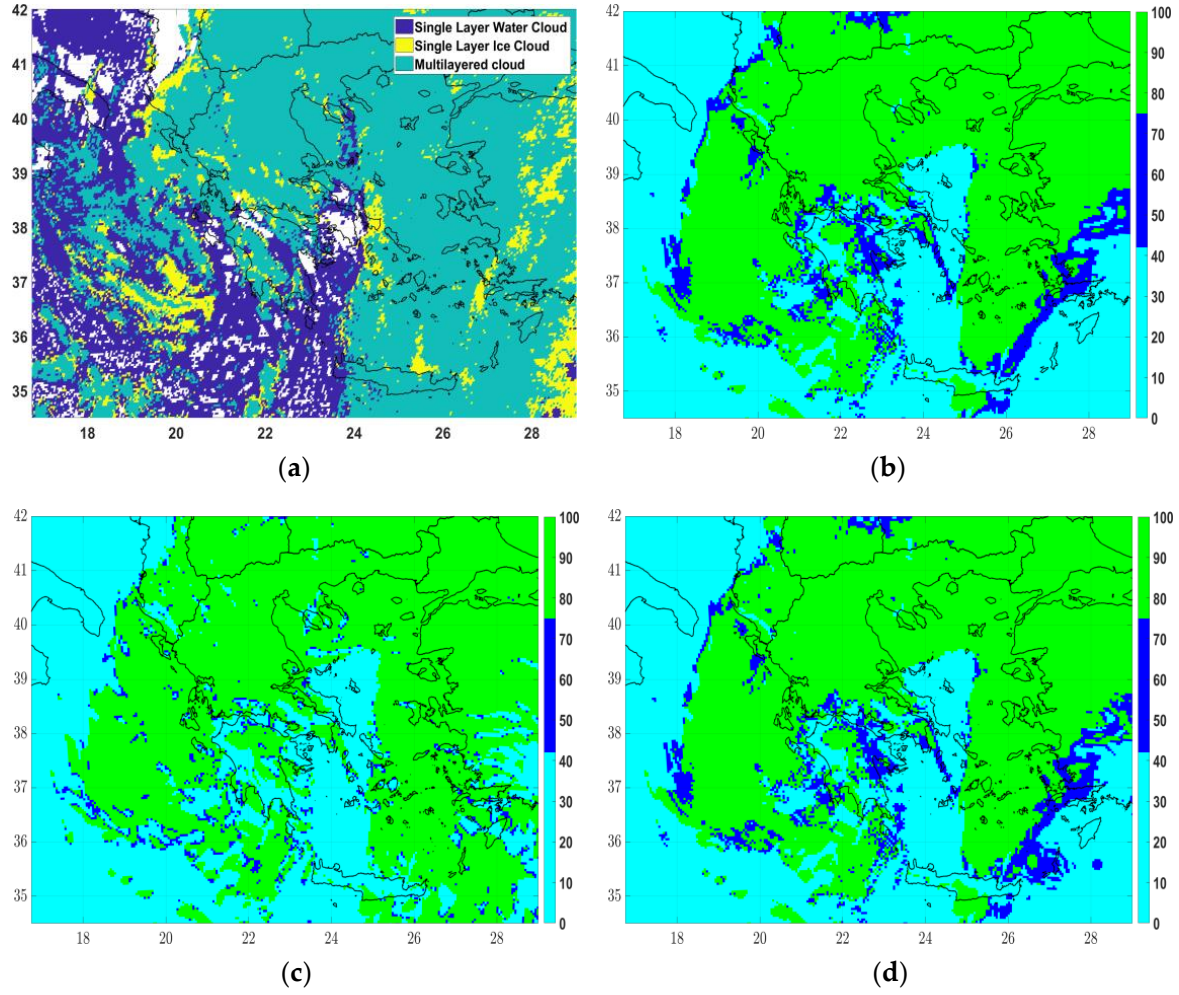


Figure 15. Comparison of (**a**) satellite cloud phase fields, with the maximum icing severity fields corresponding to "none-light" (cyan), "moderate" (blue) and "severe" (light green) for (**b**) IP_{S0}; (**c**) IP_{S2}; and (**d**) IP_{S3} on 12 March 2019 18UTC.

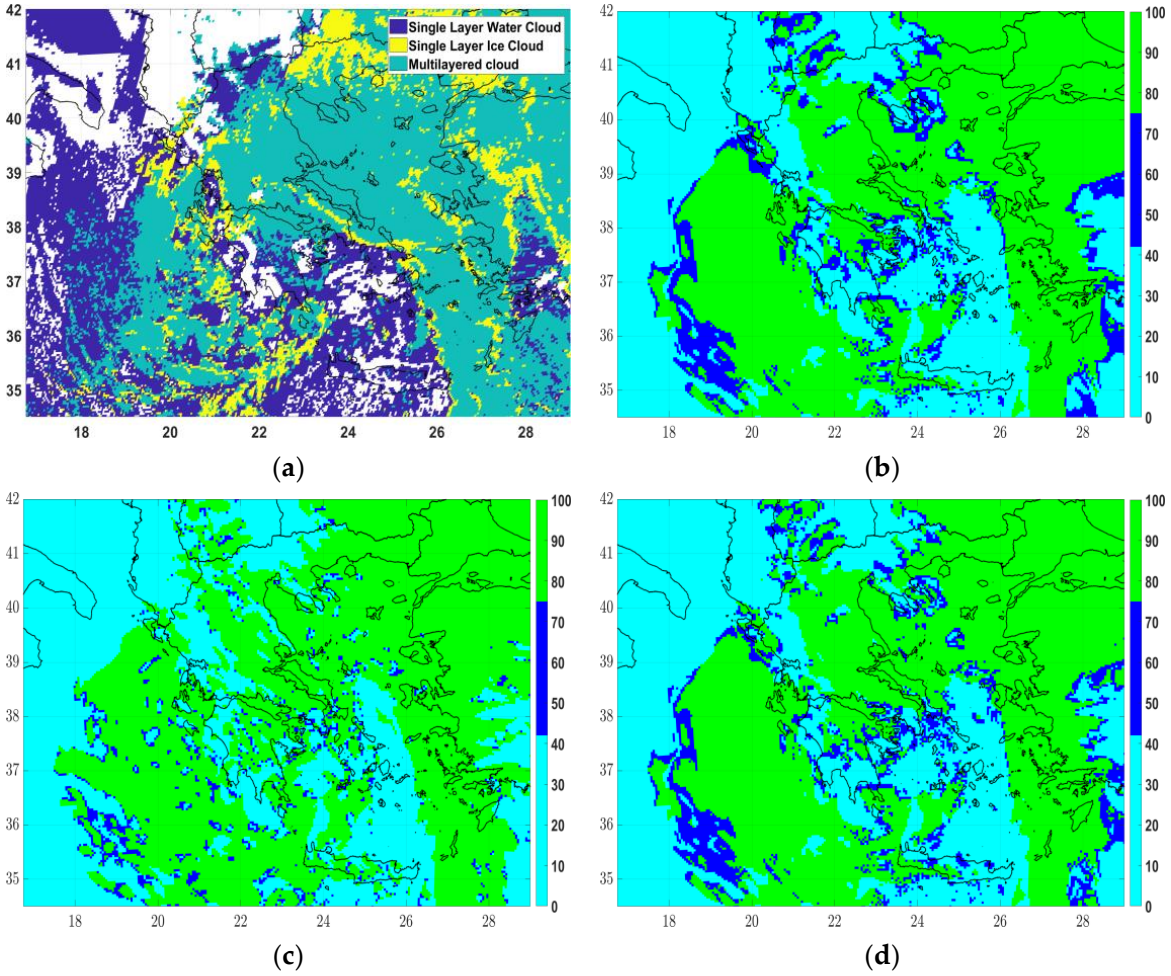


Figure 16. Comparison of (**a**) satellite cloud phase fields, with the maximum icing severity fields corresponding to "none-light" (cyan), "moderate" (blue) and "severe" (light green) for (**b**) IP_{S0}; (**c**) IP_{S2}; and (**d**) IP_{S3} on 13 March 2019 00UTC.

Looking at the IP fields at all times, moderate to severe icing existed in areas that seem to coincide with satellite multi-cloud phases, with those areas being more extensive, especially for the scenarios with the greatest M_{vv} influence (S2 and then S3). This general picture was in accordance with previous studies that have shown that severe icing occurs in the absence of high ice content (e.g., [16,31]).

It has been argued that cumuliform middle clouds and convective clouds are generally mixed-phase clouds, while low-level stratiform clouds are liquid-dominant clouds [16]. Supercooled water is frequently observed near storm tracks. In fact, the dynamic forcing plays a key role in the maintenance of the mixed phase in convective clouds. In that case even moderate vertical velocities may be associated with the growth of supercooled water and mixed-phase clouds [32]. Therefore, in the present synoptic case study, the satellite multi-layer cloud phase is expected to correspond to mixed-phase clouds with the vertical velocity having significant effect in the growth of SWDs and hence in icing formation, which is captured by the IPA results. In addition, the large extent of icing severity coincides with the multi-cloud phase, which is in agreement with other studies that have indicated large number of cases with mixed cloud-top phase [16,33].

4.2. Comparison with Radar Observations

It has been found that satellites are unable to detect any supercooled liquid cloud that may be located below thick ice clouds [15]. For this reason, the data resulted from satellite images are often accompanied by ground remote sensing observations. In our

case, radar data were retrieved and analyzed from Larisa radar located at the center of mainland Greece (white dot in Figure 17) in order to investigate the developed convective meteorological conditions around that area. Depicted radar data on 12 March 2019 at 1155 UTC (Figure 17a) suggest that there were several areas of thunderstorm events in various locations over central Greece with the precipitation activity expanding over the whole area at 1758 UTC (Figure 17b).

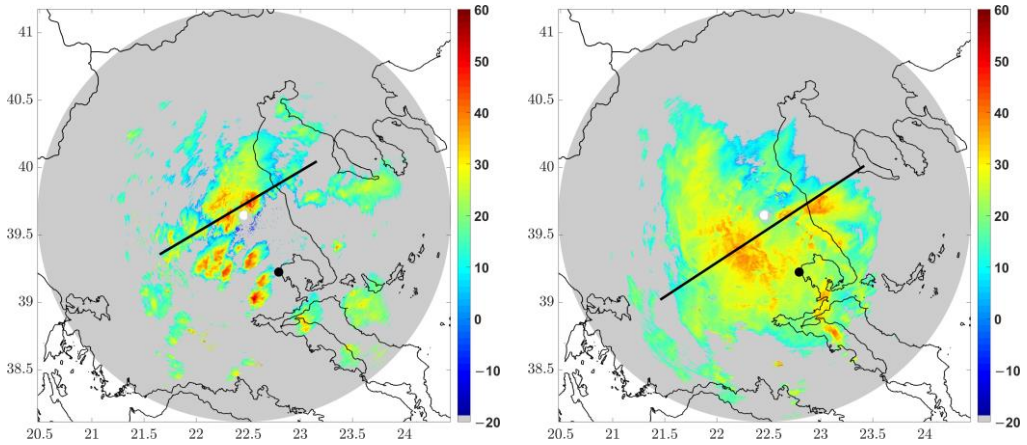
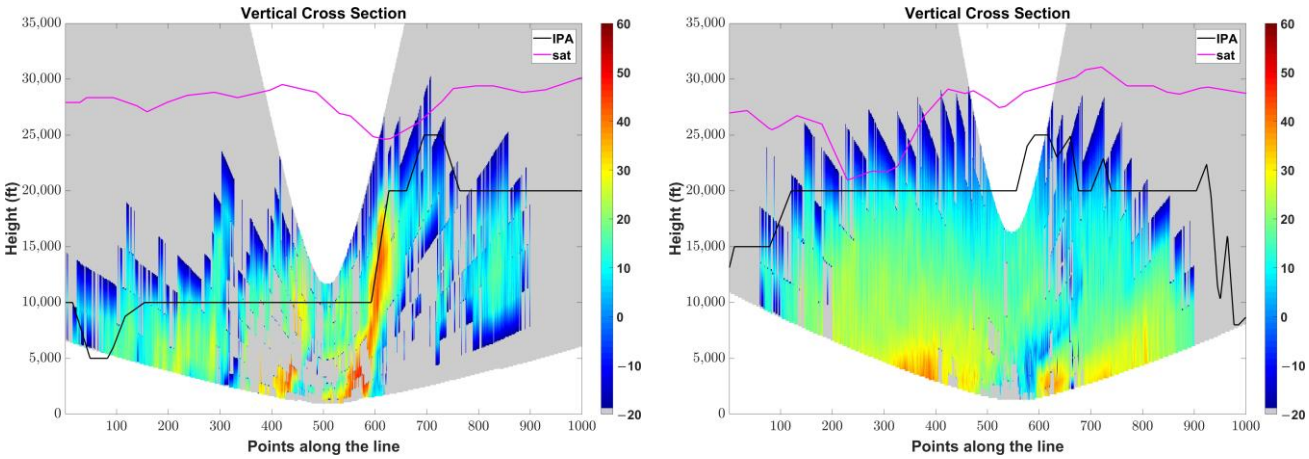


Figure 17. Radar reflectivity images on 12 March 2019 from Larissa radar: (**a**)1155 UTC and (**b**) 1758UTC. The bold lines indicate the cross sections 1 (left image) and 2 (right image) that were used for extracting further discussion, while the colored dots indicate the location of Larissa radar (white northern dot) and Nea Aghialos airport (black dot).

From these images two arbitrary cross sections were extracted, each for every time, passing through convective cells, in order to analyze the vertical extent of the convective activity and its association with possible icing presence. A radius of 25 km was selected centered over the airport, suggesting a cone shaped atmospheric column up to 45,000 feet. The same cone shaped area was selected for the IPA results (in model resolution). The maximum value of each level was selected, both for radar data and the IPA results. The IPA results used for comparison were initially the IPA CTH. At the same time, the satellite CTH was still used for comparison with the radar data and the IPA forecasts. Figure 18 illustrated the data at the two cross sections. It seems that the radar reflectivity exceeded lower height than the satellite CTH, a fact that may result from different factors such as the different sensor resolution or the algorithms used to retrieve the cloud height observation by the satellites [34]. It was argued that the detection of cloud tops for passive satellite sensors was influenced by the type of the cloud and cloud overlapping (e.g., [35,36]). In our case, it was revealed that a large fraction of the clouds included multi-layer clouds, hence this may explain the differences between the two observation datasets and where and when they exist; however, the comparison of remote sensing tools is not within the scope of this paper. Figure 18a shows that along the cross section 1 the IPA CTH was relatively close to the vertical extent of the radar data, while at the location of the greatest convectivity (near the center of the cross section) it followed generally the increase in the dBz intensity (greater than 37 dbz), where probably CB clouds with thunderstorms were present [37]. At cross section 2 on 12 March 2019 at 18UTC (Figure 18b), the radar reflectivity maxima were exhibited at lower levels and the general picture was more uniform compared with that at cross section 1 at 12UTC when the convective cells were more isolated and stronger in intensity. IPA CTH seemed to agree with the higher extent of the radar data also at that time, as their difference from satellite CTH was less than 5000 ft at locations across the line.



(**a**) (**b**)

Figure 18. Cross section of radar reflectivity fields (in dBz) from Larissa radar, the corresponding satellite CTH (purple line) and the estimated CTH from IPA (black line) on 12 March 2019 at (**a**) 12UTCand cross section 1 and (**b**) 18UTCand cross section 2.

In order to further add to our discussion, the IP values for the selected three scenarios (IP_{S0}, IP_{S2}, IP_{S3}) were plotted in the same way as the radar reflectivity in the previous graphs at the same cross sections, having still in the graph the satellite CTH just for keeping the comparison. In Figure 19, the results at cross section 1 at 12UTC are presented for the three scenarios. It was shown that the highest IP intensity was mainly between 5000 ft and 10,000 ft throughout the cross section, with some exceptions where the extension of the clouds was predicted lower or where the base of the clouds was estimated to be higher. It is also suggested that at the northeast part of cross section1, where the most intense convectivity was observed by the radar data, the algorithm predicted icing to extend to higher levels up to 20,000 ft and 25,000 ft, with the possible appearance of multi-layer clouds, for the S0 scenario with values between 10–30% and of the same order for S3 scenario, while when accounting for the greater effect of vertical velocity (scenario S2) reaching higher values (more than 60%).

Looking at cross section2 at 18UTC (Figure 20), the three IP scenarios showed in general similar behavior as at cross section 1 at 12 UTC, with the IP_{S2} being slightly different than IP_{S0} and IP_{S3} regarding the location and the areas covered by the icing rather than its intensity, especially at the northeast part of the section.

As the results of the IPA are based on the COSMO-GR NWPs, it is worth exploring the behavior of vertical velocity at the selected cross sections. Figure 21 illustrates the vertical velocity in the form of omega (ω), as was implemented by the membership function, at cross sections 1 and 2 on 12 March 2019 at 12UTC and 18UTC, respectively, together with the corresponding satellite cloud top height. It is reminded that negative ω corresponds to upward air motion, thus at 12 UTC (Figure 21a) COSMO-GR predicted upward and downward air motion alongside to each other (mainly from point 250 to 550) at cross section 1 within the first 10,000 ft from the surface and the values of ωexceeded -1.5 Pa s^{-1} or +1 Pas^{-1}. This pattern is indicative of local convective cells within these areas. On the other hand, at 18 UTC (Figure 21b) ω exhibited higher negative values exceeding -1.5 Pa s^{-1} that expanded over the largest part of cross section 2 (from point 200 to point 850), suggesting more intense convectivity over the region. This is in accordance with the radar reflectivity observed showing the phenomenon expanded and was more active over that part of central Greece (Figure 17b), suggesting vertically developed clouds (up to approximately 25,000 ft) associated with icing formation, as already discussed. Hence, since vertical velocity seems to be a key parameter in the simulations of the particular synoptic situation, its effect on in-flight icing and its relationship with various cloud types and convectivity needs further investigation and is one of the future plans of our research.

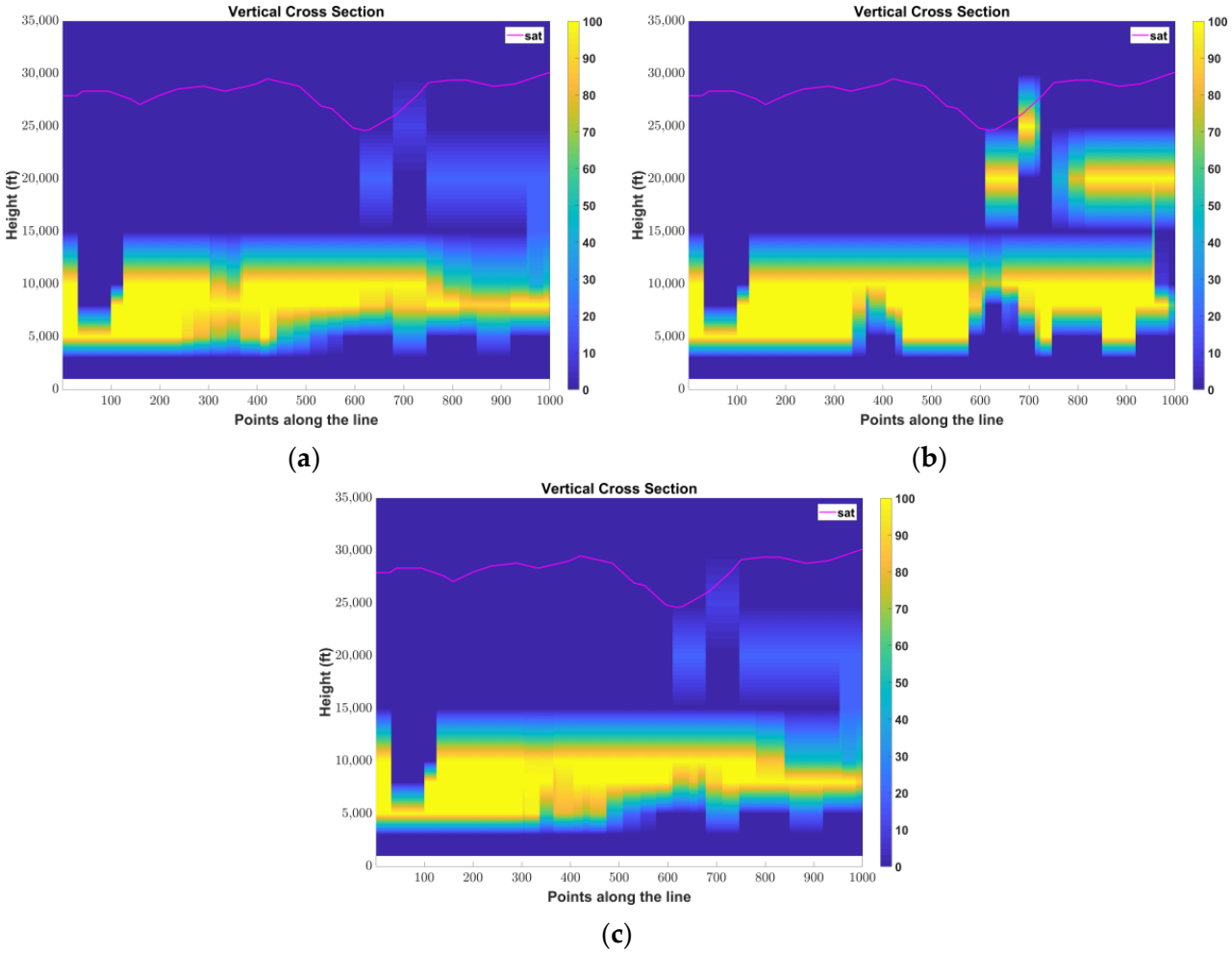


Figure 19. IP images at cross section 1 together with the corresponding satellite CTH (purple line on 12 March 2019 at 12UTC for (**a**) IP_{S0}, (**b**) IP_{S2} and (**c**) IP_{S3}.

For further investigating the similarities or differences in the behavior of the estimated IPs with the radar reflectivity, point direct comparison was made between the IPA different scenarios and the maximum reflectivity resulting from the Larissa radar over the LGBL airport (located south of the Larissa airport as presented in Figure 17) in a radar radius of 25 km. The vertical profiles with the three IP scenarios seemed to be identical over LGBL at the times chosen to be presented (12 March 2019 12UTC and 18UTC), although there are differences at 06UTC, 09UTC on 12 March 2019 and 06UTC, 09UTC and 12UTC on 13 March 2019. For that reason, only the IP_{S2} was selected to be presented here. Figure 22 illustrates the vertical profile of the Larisa radar data over LGBL on 12 March 2019 at 1155UTC (Figure 22a) and at 1758UTC (Figure 22c), together with the profile of IP_{S2} at the same times. At 12UTC there was intense convective activity over the area around the airport with values greater than 40 dbz below 5000 ft with persisting large values (of the order of 30 dbz) up to 20,000 ft indicating presence of thunderstorms and hence extensive CBs around LGBL. At 18UTC, the reflectivity was slightly diminishing, although it was still around 40 dbz at the lower levels. At these hours, the IP estimates taken within the same radius of 25 km were highest between 5000 ft and 10,000 ft and 20,000 ft and 30,000 ft at 12UTC, indicating the presence of two-layer clouds existing in this area and between 5000 ft and 20,000 ft at 18UTC, all corresponding to the heights with the largest radar reflectivity.

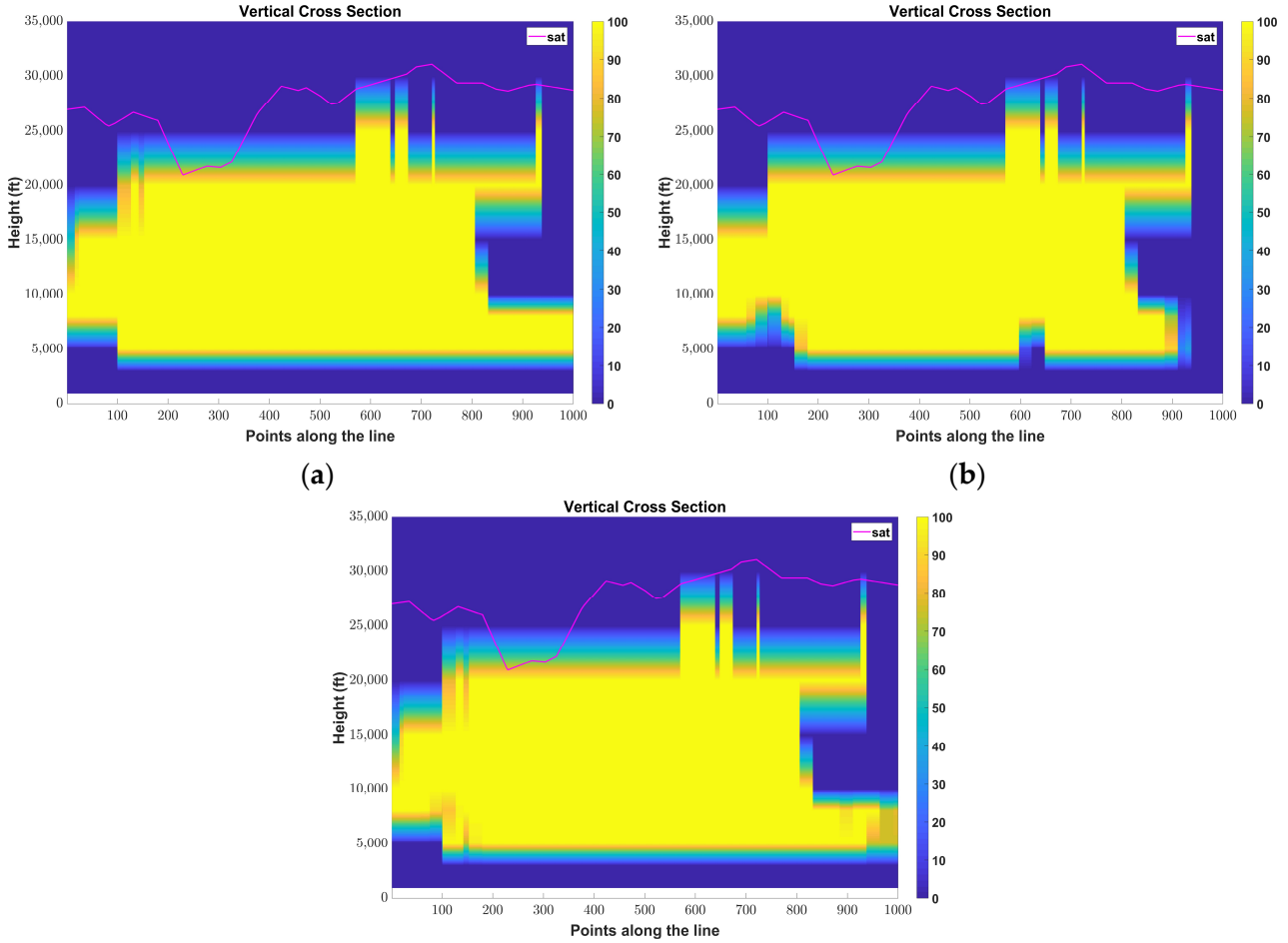


Figure 20. IP images at the cross section 2 together with the corresponding satellite CTH (purple line on 12 March 2019 at 18UTC for (**a**) IP_{S0}, (**b**) IP_{S2} and (**c**) IP_{S3}.

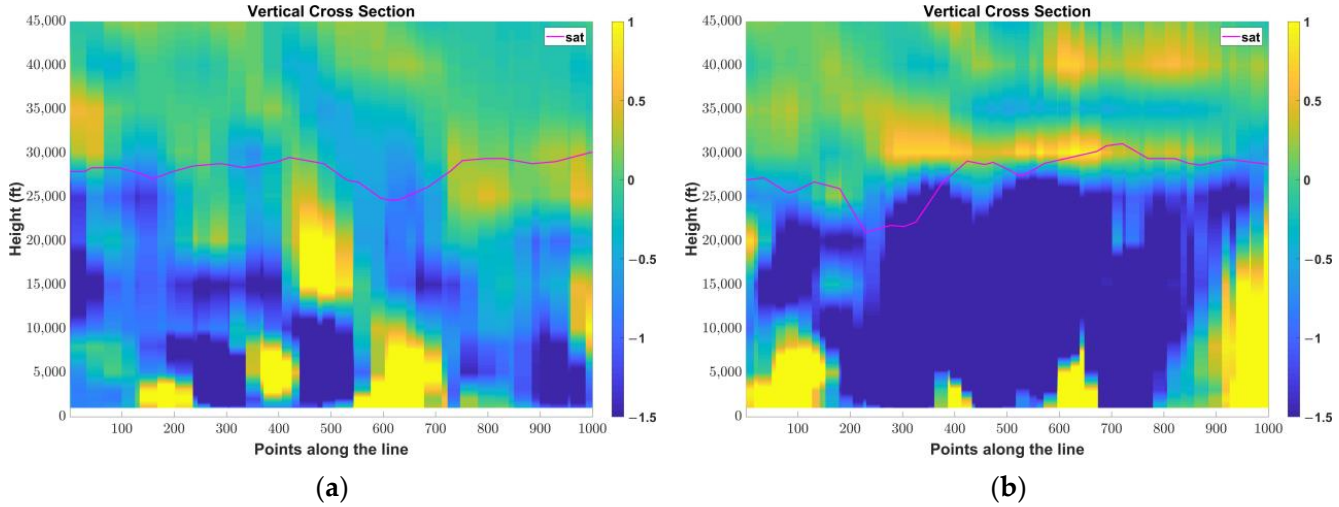


Figure 21. Vertical velocity ω as predicted by COSMO-GR at (**a**) cross section 1 on 12 March 2019 at 12 UTC and (**b**) cross section 2 on 12 March 2019 at 18 UTC together with the corresponding satellite CTH (purple line). Negative values of ω correspond to upward motion of air.

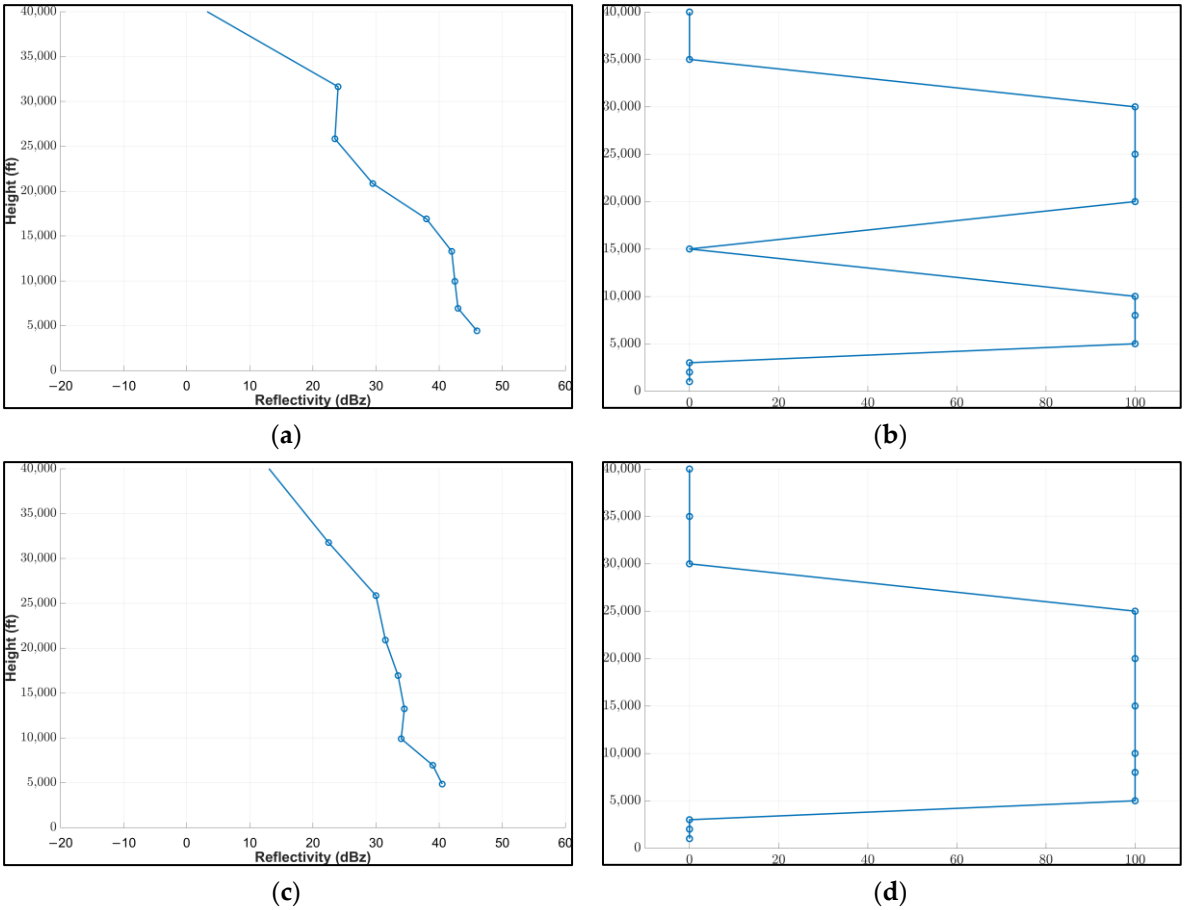


Figure 22. Vertical profiles at Nea Aghialos location (LGBL) of (**a**) Larissa radar data and (**b**) IP_{S2} on 12 March 2019 at 12UTC and (**c**) radar data and (**d**) IP_{S2}on 12 March 2019 at 18UTC within a radius of 25 km. The horizontal axis of the radar data is in dBz and of the IP in percentage, while the vertical axes are in feet.

4.3. Comparison with METARs

In the present case study, the METARs were also used as an additional source to retrieve information on the height of the cloud base as well as the type of cloud. All METAR observations at Nea Aghialos airport (LGBL) on 12 March 2019 for the period between 1150UTC and 2350UTC are included in Appendix A. It should be noted that no radio data are available for this site. It is shown (Table A1) that during all relevant hours on 12 March 2019, the cloud base was as low as 1000 ft to 1500 ft with the convective clouds (CB and/or TCU), having their bases at 1500 ft–2000 ft covering 1–2/8 of the sky (FEW in Table A1) and most of the time being accompanied by thunderstorms, thus no freezing rain was recorded. These clouds are possibly embedded within layered low and middle clouds with "broken-BKN" or "overcast-OVC" sky coverage, as announced in the METARs. Air temperature at the surface was initially as high as 14 °C, falling rapidly to 8 °C at around 1600 UTC as the cold air of the cold front passed through the area of the airport and the day progressed. Hence, the IPA predictions of cloud base heights and the large potential presence of icing at heights as low as 5000 ft was in accordance with these observations at the selected times.

4.4. The Dynamics of IPA in Investigating In-Flight Icing

The IPA method was mainly based on the FIP method by [12] identifying different meteorological situations and effects and was further expanded by implicating weights on certain membership functions based on the general idea by [13] on the SFIP, which is

in turn based on a simplified version of FIP, but in the IPA these weights were used to further form scenarios to investigate the sensitivity of the IPA on meteorological conditions influencing the icing formation.

The IPA method was applied to investigate the in-flight icing formation during a low-pressure system passage over Greece. Although the results described are dedicated to one meteorological synoptic case, the weather conditions that are associated with this case can be generalized to similar case studies. This well-organized depression system accompanied by an occlusion and a cold and a warm front exhibited a development and motion similar to several low-pressure weather systems passing through Greece during autumn, winter and spring time (e.g., [38,39]). The results of the IPA regarding the cloud top and base heights associated with such a depression showed the development of cumuliform or convective as well as stratiform clouds, with the cumuliform or convective being present at the areas where upward vertical motion or unstable conditions were expected, i.e., at the location of the occlusion, on the frontal surface of the cold front or in front of the warm front or due to the vertical motion above its center.

The IPA showed the icing severity to increase in the vicinity of those areas due to the possible presence of such vertically extended clouds that are generally associated with the presence of SWDs within their depth. These results were supported by the satellite multi-layer cloud phase images that revealed mixed phase clouds over those areas. In addition, dynamic forcing played an important role in the maintenance of the mixed phase in convective clouds, with even moderate vertical velocities promoting the growth of SWDs and mixed-phase clouds and hence increasing the potentiality of icing formation; our result indicated that the sensitivity of icing presence and intensity in the increase of vertical velocity is an important outcome. At the same time, the agreement of the IPA results on icing severity with the increase in radar dBz reflectivity supports this argument. Values of reflectivity as large as 40 dBz at certain locations, indicating presence of thunderstorms and hence extensive CBs and therefore significant vertical air motion, were associated with large IP values within the same depth of the observed radar reflectivity, with the IP values increasing when considering the effect of vertical velocity, indicating the sensitivity of icing formation to the convective motion.

Although PIREPs were not retrievable for the studied area of Greece, making a general comparison with the bibliography related with PIREPs values, the IPA method showed that IP estimates and horizontal cover is greatest between 8000 ft and 15,000 ft (Figure 10), which is in agreement with PIREPs stating that icing formation is important at altitudes around 10,000 ft, with most of the reported cases to appear between 5000 ft and 13,000 ft [1].

Thus, the IPA method can provide some useful insight to the in-flight icing formation. Certainly, the fact that this work is mainly based on qualitative evaluation with the available remote sensing and ground-point measurements makes necessary expanding the investigation to regions for which PIREPs are available in order to extract a detailed conventional quantitative statistical analysis, which will be a part of future work as described in the next section.

5. Conclusions—Suggestions

Forecasting in-flight icing conditions is a critical component of aviation safety, particularly in regions with variable and complex meteorological patterns, such as Greece. In-flight icing poses significant risks to aircraft performance, flight stability and passenger safety. Accurate forecasting enables proactive measures to mitigate these risks, ensuring safer and more efficient flight operations. This paper outlines a methodology of forecasting icing conditions over Greece that takes into consideration the meteorological scenarios related to such challenges, the advancements in NWP modeling and observation types that reveal the structure of the atmosphere.

Specifically, the Icing Potential Algorithm (IPA) is presented, which is based on a quantitative measure used to assess the likelihood of in-flight icing conditions. This index integrates various meteorological parameters, employing COSMO-GR NWP forecasts

and membership functions built in a fuzzy logic system to provide a comprehensive evaluation of atmospheric conditions that may lead to the formation of ice on aircraft surfaces. The IPA was applied to investigate the in-flight icing formation in a case of a well-organized depression system associated with occluded, cold and warm fronts during its passage over Greece. Icing was predicted to be formed at flight levels between 3000 ft and 25,000 ft over Greece, with the strongest IP values and extended IP field appearing in the range between 8000 ft and 15,000 ft. The scenarios tested indicated the importance of the effect of various meteorological parameters, namely the cloud presence and the associated precipitation types, the cloud liquid water content and the vertical velocity, either alone or in combinations among them. Hence, among the six scenarios investigated, it was suggested that apart from the cloud presence and the precipitation type (S0), the vertical velocity (S2) was largely significant in influencing IP values over Greece in this particular meteorological situation, for which convectivity was a dynamic condition leading to significant vertical airflows with direct effects on vertically extensive cloud development and thunderstorm occurrence.

In the absence of a PIREP retrieval database over Greece, the evaluation and discussion performed in this work cannot be fully quantified with statistical analysis. The direct qualitative comparison of CTH diagnosed by the IPA with satellite extracted indicated underestimation by IPA. However, these datasets originate from numerically different methods and characteristics and their direct comparison was expected to give differences. The IPA was structured mainly to account for the effects of clouds whose presence possibly enhances icing formation, while the satellite-based retrievals were influenced by the type of the cloud and cloud overlapping, and their passive sensors were unable to detect supercooled liquid cloud that may be located below thick ice cloud, hence the CTH values were expected to be different among the two datasets. The use of satellite CP fields and their connection with IP severity resulting from the different IP scenarios, especially for S2, revealed that the greatest IP intensity was associated with single-layer ice and multi-layer clouds that were comprised of both ice and supercooled water.

On the other hand, comparison with radar reflectivity showed that the IPA results were closer to the vertical extent of the reflectivity, when considering cross sections passing from convective activity, or above a point of increased convection. The interrelation of the radar reflectivity with the IP scenarios showed that the greatest IP intensity appeared at the locations with higher reflectivity, especially for the S2 scenario, dependent significantly on the vertical velocity. This may be related to the fact that the mixed phase convective clouds present near the storms developed in the particular synoptic situation, as also pointed out by the point ground measurements, were characterized by thermal and dynamic instability, which in turn influenced the presence of supercooled water and hence icing formation.

The sensitivity of the presence and intensity of in-flight icing to the vertical velocity, the convective activity and the various cloud types requires further investigation and is part of future work. The IPA method has been so far used for research purposes and one big effort is performed with the present work. The scope of applying it over Greece is that this geographical region is topographically complex with weather conditions influenced also by local effects and with notable aviation traffic of both commercial and general aviation operations, and this was the first comprehensive attempt to apply an icing code over the region. Although the case study investigated is characteristic of the area of Eastern Mediterranean and similar case studies are expected to result in similar outcomes, if this method is to be used operationally, it requires expanding its employment to other case studies. For this reason, various meteorological synoptic conditions potentially associated with icing formation will be examined. For example, other organized depressions of different origins will be investigated over Greece in the autumn, winter and early spring time when the atmosphere exhibits low temperatures and/or significant convective activity. On the other hand, the necessity to expand the evaluation of the IPA to include PIREPs that are not retrievable over Greece makes it essential to apply the method to other geographical regions. In this way, the verification of the method will be reinforced with the conventional

quantitative statistical analysis by applying the IPA over areas where retrieval of PIREP databases is available.

Author Contributions: Conceptualization, P.L.; methodology, P.L.; software, P.L.; validation, I.S. and F.G.; formal analysis, P.L. and I.S.; investigation, P.L.; data curation, P.L., I.S. and F.G.; writing—original draft preparation, P.L.; writing—review and editing, P.L., I.S. and F.G; visualization, I.S. All authors have read and agreed to the published version of the manuscript.

Funding: This research received no external funding.

Institutional Review Board Statement: Not applicable.

Data Availability Statement: The data presented in this study are available on request from the corresponding author.

Conflicts of Interest: The authors declare no conflicts of interest.

Appendix A

The METAR observations from Nea Aghialos airport (LGBL) are presented here during the period 1150UTC to 2350UTC on 12 March 2019 (Table A1). An example of METAR decoding is given here, that at 1220UTC (121220Z), e.g.,

METAR LGBL 121220Z 09009KT 9999 VCTS FEW018CB FEW020TCU SCT030 BKN080 14/09 Q1004=

in which it is mentioned that in the vicinity of the airport thunderstorms were observed (VCTS) with the clouds above the airport being convective cumulonimbus with base at 1800 ft and 1–2/8 sky cover (FEW018CB), convective towering cumulus with base at 2000 ft and 1–2/8 sky cover (FEW020TCU), possibly "hidden" by layered low clouds at 3000 ft with 3–4/8 sky cover (SCT030)and middle clouds at 8000 ft with 5–7/8 sky cover (BKN080), while air temperature was 14 °C. These types of clouds remained over the airport during the whole period and at several times thunderstorms developed (TSRA). The lowest cloud base was observed from 1550 UTC–1650 UTC at 1000 ft and 1–2/8 sky cover (FEW010). Temperature fell progressively after 1350 UTC down to 7 °C at 1720UTC, remaining approximately constant until the end of the selected period.

Table A1. METAR observations at Nea Aghialos (LGBL) airport between 1150UTC and 2350UTC on 12 March 2019 every half hour. Thunderstorm and clouds are highlighted in bold. Dataset retrieved from mesonet.agron.iastate.edu/ accessed on 24 January 2024.

LGBL METAR OBSERVATIONS
METAR LGBL 122350Z 01010G20KT 9999 **FEW020TCU BKN025 OVC080** 08/03 Q1011=
METAR LGBL 122250Z 35018G28KT 9999 **-RA FEW020TCU BKN025 OVC080** 07/03 Q1010=
METAR LGBL 122150Z 35012KT 9999 -RA **FEW020TCU BKN025 OVC080** 08/03 Q1009=
METAR LGBL 122050Z 35017G27KT 6000 -RA **FEW020TCU BKN025 OVC080** 07/03 Q1008=
METAR LGBL 121950Z 01012KT 6000 -RA **FEW020TCU BKN025 OVC080** 07/04 Q1008=
METAR LGBL 121850Z 33013KT 6000 -RA **FEW020TCU BKN025 OVC080** 07/03 Q1007=
METAR LGBL 121820Z 02010G20KT 6000 **-TSRA FEW018CB FEW020TCU BKN025 OVC080** 07/04 Q1007=
METAR COR LGBL 121750Z 02016KT 6000 **-TSRA FEW018CB FEW020TCU BKN025 OVC080** 07/04 Q1006=
METAR LGBL 121720Z 02017G27KT 9999 **FEW020TCU BKN025 OVC080** 07/04 Q1005=
METAR LGBL 121650Z 02017KT 7000 -RA **FEW010 FEW020TCU BKN025 OVC080** 08/05 Q1004=
METAR LGBL 121620Z 35009KT 5000 -RA **FEW010 FEW020TCU BKN025 OVC080** 09/06 Q1004=
METAR LGBL 121550Z 27008KT 5000 -RA **FEW010 FEW020TCU SCT030 BKN080** 11/06 Q1004=
METAR LGBL 121520Z 34009KT 9999 -RA **FEW020TCU SCT030 BKN080** 11/06 Q1004=
METAR LGBL 121450Z 01009KT 9999 -RA **FEW020TCU SCT030 BKN080** 11/06 Q1004=
METAR LGBL 121420Z 10009KT 9999 -RA **FEW020TCU SCT030 BKN080** 12/08 Q1004=
METAR LGBL 121350Z 10014KT 9999 **FEW020TCU SCT030 BKN080** 13/07 Q1004=
METAR LGBL 121320Z 10012KT 9999 **FEW020TCU SCT030 BKN080** 14/08 Q1003=
METAR LGBL 121250Z 11010KT 9999 **VCTS FEW018CB FEW020TCU SCT030 BKN080** 14/08 Q1004=
METAR LGBL 121220Z 09009KT 9999 **VCTS FEW018CB FEW020TCU SCT030 BKN080** 14/09 Q1004=
METAR LGBL 121150Z 06006KT 9999 **FEW015 SCT030 BKN080** 13/08 Q1004=

References

1. Schultz, P.; Politovich, M.K. Toward the improvement of aircraft-icing forecasts for the continental United States. *Weather Forecast.* **1992**, *7*, 491–500. [CrossRef]
2. Kalinka, F.; Roloff, K.; Tendel, J.; Hauf, T. The In-flight icing warning system ADWICE for European airspace—Current structure, recent improvements and verification results. *Meteorol. Z.* **2017**, *26*, 441–455. [CrossRef]
3. Cober, S.G.; Isaac, G.A.; Strapp, J.W. Characterizations of aircraft icing environments that include supercooled large drops. *J. Appl. Meteorol.* **2001**, *40*, 1984–2002. [CrossRef]
4. Köler, F.; Görsdorf, U. Towards 3D prediction of supercooled liquid water for aircraft icing: Modifications of the microphysics in COSMO-EU. *Meteorol. Z.* **2014**, *23*, 253–262. [CrossRef]
5. Bruno, O.; Hoose, C.; Storelvmo, T.; Coopman, Q.; Stengel, M. Exploring the cloud top phase partitioning in different cloud types using active and passive satellite sensors. *Geophys. Res. Lett.* **2020**, *48*, e2020GL089863. [CrossRef]
6. Green, S.D. Astudyof U.S. Inflight Icing Accidents, 1978 to 2002. In Proceedings of the 44th AIAA Aerospace Sciences Meeting and Exhibit, AIAA, Reno, NV, USA, 9–12 January 2006.
7. Politovich, M.K. Aircraft icing caused by large supercooled droplets. *J. Appl. Meteorol. Climatol.* **1989**, *28*, 856–868. [CrossRef]
8. McDonough, F.; Wolff, C.A.; Politovich, M.K. Forecasting supercooled large drop icing conditions. In Proceedings of the 13th Conference on Aviation, Range and Aerospace Meteorology, New Orleans, LA, USA, 11–15 January 2008.
9. Hansman, R.J. Droplet size distribution effects on aircraft ice accretion. *J. Aircr.* **1985**, *22*, 503–508. [CrossRef]
10. Politovich, M.K.; Belo-Pereira, M. *Aircraft Icing, Reference Module in Earth Systems and Environmental Sciences*; Elsevier: Amsterdam, The Netherlands, 2019; ISBN 9780124095489. [CrossRef]
11. Francis, P. Detection of aircraft icing conditions over Europe using SEVIRI data. In Proceedings of the 2007 EUMETSAT Meteorological Satellite Conference and the 15th AMS Satellite Meteorology and Oceanography Conference, Amsterdam, The Netherlands, 24–28 September 2007; p. 8. Available online: https://www.eumetsat.int/joint-2007-eumetsat-and-american-meteorological-society-conference (accessed on 10 March 2022).
12. McDonough, F.; Bernstein, B.C.; Politovich, M.K.; Wolff, C.A. The forecast icing potential (FIP) algorithm. In Proceedings of the 20th International Conference on Interactive Information Processing Systems (IIPS) for Meteorology, Oceanography and Hydrology, Seattle, WA, USA, 11–15 January 2004.
13. Belo-Pereira, M. Comparison of in-flight aircraft icing algorithms based on ECMWF forecasts. *Meteorol. Appl.* **2015**, *22*, 705–715. [CrossRef]
14. Thompson, G.; Politovich, M.K.; Rasmussen, R.M. A numerical weather model's ability to predict characteristics of aircraft icing environments. *Weather. Forecast.* **2017**, *32*, 207–221. [CrossRef]
15. Morcrette, C.; Brown, K.; Bowyer, R.; Gill, P.; Suri, D. Development and Evaluation of In-Flight Icing Index Forecast for Aviation. *Weather. Forecast.* **2019**, *34*, 731–750. [CrossRef]
16. Casqueiro, B.C.; Trigo, I.; Belo-Pereira, M. Characterization of icing conditions using aircraft reports and satellite data. *Atmos. Res.* **2023**, *293*, 106884. [CrossRef]
17. Balwin, M.; Treadon, R.; Contorno, S. Precipitation type prediction using a decision tree approach with NMC's mesoscale ETA Model. In Proceedings of the 10th AMS Conference on Numerical Weather Prediction, Portland, OR, USA, 18–22 July1994.
18. Politovich, M.K.; McDonough, F.; Bernstein, B.C. Issues in forecasting icing severity. In Preprints. In Proceedings of the 10th Conference on Aviation, Range and Aerospace Meteorology, Portland, OR, USA 12–16 May 2002; American Meteorological Society: Boston, MA, USA; pp. 85–89.
19. Steppeler, J.; Doms, G.; Schättler, U. Meso-gamma scale forecasts using the nonhydrostatic model LM. *Meteorol. Atmos. Phys.* **2003**, *82*, 75–96. [CrossRef]
20. Doms, G.; Forstner, J.; Heise, E.; Herzog, H.J.; Mironov, D.; Raschendorfer, M.; Reinhardt, T.; Ritter, B.; Schrodin, R.; Schultz, J.P.; et al. *A Description of the Nonhydrostatic Regional COSMO MODEL. Part II: Physical Parameterization*; 2011. Available online: http://www.cosmo-model.org (accessed on 5 November 2021).
21. Baldauf, M.; Seifert, A.; Förstner, J.; Majewski, D.; Raschendorfer, M.; Reinhardt, T. Operational convective-scale numerical weather prediction with the COSMO model: Description and sensitivities. *Mon. Weather Rev.* **2011**, *139*, 3887–3905. [CrossRef]
22. Schättler, U.; Doms, G.; Schraff, C. *A Description of the Nonhydrostatic Regional COSMO Model. Part VII: User's Guide*; 2021. Available online: http://www.cosmo-model.org (accessed on 11 January 2022). [CrossRef]
23. Stengel, M.; Mieruch, S.; Jerg, M.; Karlsson, K.-G.; Scheirer, R.; Maddux, B.; Meirink, J.F.; Poulsen, C.; Siddans, R.; Walther, A. The Clouds Climate Change Initiative: The Assessment of State of the Art Cloud Property Retrieval Systems Applied to AVHRR heritage measurements. *Remote Sens. Environ.* **2014**, *162*, 363–379. [CrossRef]
24. Xu, M.; Thompson, G.; Adriaansen, D.R.; Landolt, S.D. On the Value of Time-Lag-Ensemble Averaging to Improve Numerical Model Predictions of Aircraft Icing Conditions. *Weather Forecast.* **2019**, *34*, 507–519. [CrossRef]
25. Wandishin, M.S.; Etherton, B.; Hart, J.; Layne, G.; Petty, M.A. Assessment of the HiRes Current Icing Project (CIP) and Forecast Icing Project (FIP). NOAA: Silver Spring, Maryland, 2013. [CrossRef]

26. Huffman, G.J.; Bolvin, D.T.; Braithwaite, D.; Hsu, K.L.; Joyce, R.J.; Kidd, C.; Nelkin, E.J.; Sorooshian, S.; Stocker, E.F.; Tan, J.; et al. Integrated Multi-satellite Retrievals for the Global Precipitation Measurement (GPM) mission (IMERG). Chapter 19. In *Satellite Precipitation Measurement. Advances in Global Change Research*; Levizzani, V., Kidd, C., Kirschbaum, D.B., Kummerow, C.D., Nakamura, K., Turk, F.J., Eds.; Springer Nature: Dordrecht, The Netherlands, 2020; Volume 67, pp. 343–353, ISBN 978-3-030-24567-2. [CrossRef]
27. Le Bot, C. *SIGMA: System of Icing Geographic Identification in Meteorology for Aviation*; SAE Technical Paper 2003-01-2085; MeteoFrance: Toulouse, France, 2003. [CrossRef]
28. Minnis, P.; Smith, W.L.J.; Nguyen, L.; Khaiyer, M.M.; Spangenberg, D.A.; Heck, P.W.; Palikonda, R.; Bernstein, B.C.; McDonough, F. A real time satellite-based icing detection system. In Proceedings of the 14th International Conference Clouds and Precipitation, Bologna, Italy, 18–23 July 2004.
29. Minnis, P.; Nguyen, L.; Smith, W.; Murray, J.J.; Palikonda, R.; Khaiyer, M.; Spangenberg, D.A.; Heck, P.W.; Trepte, Q.Z. Near real time satellite cloud products for nowcasting applications. In Proceedings of the WWRP Symp. Nowcasting & Very Short Range Forecasting, Toulouse, France, 5–9 September 2005.
30. Wolff, C.A.; McDonough, F.; Politovich, M.K.; Bernstein, B.C. *FIP Severity Technical Document*; 2006; p.26. Report submitted to the FAA Aviation Weather Research Board. Available online: http://n2t.net/ark:/85065/d7th8p76 (accessed on 4 August 2024).
31. Politovich, M.K.; Bernstein, T.A.O. Aircraft icing conditions in Northeast Colorado. *J. Appl. Meteorol.* **2002**, *41*, 118–132. [CrossRef]
32. Korolev, A.V.; Mcfarquhar, G.M.; Field, P.R.; Franklin, C.N.; Lawson, P.; Wang, Z.; Williams, E.; Abel, S.J.; Axisa, D.; Borrmann, S.; et al. Mixed-phase clouds: Progress and challenges. *Meteorol. Monogr.* **2017**, *58*, 5.1–5.50. [CrossRef]
33. Cober, S.G.; Isaac, G.A. Aircraft icing environments observed in mixed-phase clouds. In Proceedings of the 40th AIAA Aerospace Sciences Meeting & Exhibit, Reno, NV, USA, 14–17 January 2002. [CrossRef]
34. Liu, B.; Huo, J.; Lyu, D.; Wang, X. AssessmentofFY-4AandHimawari-8CloudTopHeightRetrievalthroughComparisonwithGround-BasedMillimeterRadaratSitesinTibetandBeijing. *Adv. Atmos. Sci.* **2021**, *38*, 1334–1350. [CrossRef]
35. Naud, C.M.; Muller, J.-P.; Clothiaux, E.E.; Baum, B.A.; Menzel, W.P. Intercomparison of multiple years of MODIS, MISR and radar cloud-top heights. *Ann. Geophys.* **2005**, *23*, 2415–2424. [CrossRef]
36. Yang, X.; Ge, J.; Hu, X.; Wang, M.; Han, Z. Cloud-Top Height Comparison from Multi-Satellite Sensors and Ground-Based Cloud Radar over SACOL Site. *Remote Sens.* **2021**, *13*, 2715. [CrossRef]
37. Schilke, C.; Hecker, P. Dynamic route optimization based on adverse weather data. In Proceedings of the 4th SESAR Innovation Days, Madrid, Spain, 25–27 November 2014.
38. Maheras, P.; Flocas, H.A.; Patrikas, I.; Anagnostopoulou, C. A 40-year objective climatology of surface cyclones in the Mediterranean region: Spatial and temporal distribution. *Int. J. Climatol.* **2001**, *21*, 109–130. [CrossRef]
39. Cartalis, C.; Chrysoulakis, N.; Feidas, H.; Pitsitakis, N. Categorization of cold period weather types in Greece on the basis of the photointerpretation of NOAA/AVHRR imagery. *Int. J. Remote Sens.* **2004**, *25*, 2951–2977. [CrossRef]

Disclaimer/Publisher's Note: The statements, opinions and data contained in all publications are solely those of the individual author(s) and contributor(s) and not of MDPI and/or the editor(s). MDPI and/or the editor(s) disclaim responsibility for any injury to people or property resulting from any ideas, methods, instructions or products referred to in the content.